Transactions on Emerging Telecommunications Technologies

WILEY

RESEARCH ARTICLE OPEN ACCESS

A Joint Channel Modeling, Parameter Estimation and Geometry-Based Indoor Localization for 5G Systems

Paulo Francisco da Conceição[1,2] | Rodrigo Pinto Lemos[1,3] | Flávio Geraldo Coelho Rocha[1,3]

[1]Excellence Center in Smart Wireless Networks and Advanced Services (CERISE), Federal University of Goiás (UFG), Goiânia, Brazil | [2]Department of Computer Science, Federal Institute of Goiás (IFG), Inhumas, Brazil | [3]Department of Electrical, Computer, and Mechanical Engineering, Federal University of Goiás (UFG), Goiânia, Brazil

Correspondence: Paulo Francisco da Conceição (paulo.conceicao@ifg.edu.br)

Received: 15 August 2023 | **Revised:** 26 December 2025 | **Accepted:** 20 May 2026

Keywords: 5G | indoor localization | mMIMO | mmWave

ABSTRACT

This work proposes a Mobile Station (MS) localization method for indoor environments using a single Base Station (BS) equipped with a massive Multiple-Input Multiple-Output (mMIMO) antenna array. The proposal can be divided into three main stages: (1) channel modeling, (2) estimation of localization parameters, and (3) estimation of MS position. We consider a millimeter-Wave (mmWave) mMIMO channel model to estimate five localization parameters: Time of Arrival (ToA), two-dimensional Angle of Departure (2D-AoD)-azimuth and elevation, and two-dimensional Angle of Arrival (2D-AoA)-azimuth and elevation. Then, from AoA and AoD data, the proposed method can analyze the various transmission paths and identify whether there is a Line-of-Sight (LoS) path, allowing the automatic determination and application of the most suitable localization algorithm. The system model is comprehensive, approaching a 5G small cell with mmWave and mMIMO technologies transmitting in an indoor environment with LoS and Non-Line-of-Sight (NLoS) conditions and multiple Scatterers. Simulations are carried out, and the results are compared to those of three related methods present in the literature. The obtained results demonstrate that the proposed method achieves sub-metric accuracy under LoS conditions and outperforms related methods in NLoS conditions. Additionally, the proposed method is simpler, faster, and relies on a single BS for localization.

1 | Introduction

Data transmission at millimeter-wave (mmWave) and massive Multiple-Input Multiple-Output (mMIMO) are some of the main 5G enabling technologies [1, 2]. The mmWave operates with carrier frequencies beyond 24 GHz and can offer an extremely wide bandwidth. Such bandwidth allows for a finer degree of time-delay resolution, providing an improved Time of Arrival (ToA) estimation. The large-scale antenna arrays used in mMIMO provide simultaneous transmissions and spatial multiplexing while offering a high angular resolution and improved estimation of Angle of Arrival (AoA) and Angle of Departure (AoD) [3, 4].

Greater precision in the estimation of communication channel parameters, such as ToA, AoD, and AoA, enables applications that require precise localization, for example, navigation, geo-marketing, asset tracking, augmented reality, and indoor localization [5–7]. Taking into account scenarios and perspectives for 5G and beyond 5G (B5G) networks in the upcoming years, it is envisioned that a high accuracy will be required for indoor localization, such as in services related to the Internet of Things (IoT) and Industry-4.0 [8–10]. Another application for indoor environments is related to the accessibility of people with visual impairments. In this case, the precise localization using only the cellular network facilitates the development of applications for mobile devices. These applications might be

https://doi.org/10.1002/ett.70456

able to guide, inside a building, visually impaired people to their destination, providing independence and improving life quality [11, 12].

Although many approaches have been proposed to improve localization accuracy in Mobile Stations (MSs) for indoor environments, significant challenges remain [5, 13, 14]. Existing methods often require specialized resources that are not available in standard cellular networks, such as fingerprint databases for precise indoor mapping, or Round-Trip Time (RTT)-based distance calibration for enhanced ranging accuracy, making them impractical for real-world applications [15–17]. Furthermore, many solutions assume a Line-of-Sight (LoS) condition or require multiple Base Stations (BSs) to achieve sub-metric accuracy, which limits their scalability and applicability [18, 19].

This work addresses these limitations by proposing a localization method that operates solely within the existing cellular network infrastructure. Our approach uses only one BS equipped with a MIMO antenna array and achieves sub-metric accuracy, addressing both LoS and Non-Line-of-Sight (NLoS) scenarios. For such a purpose, we propose a localization method in three main stages: (1) channel modeling, (2) estimation of localization parameters: ToA, two-dimensional Angle of Departure (2D-AoD)-azimuth and elevation, two-dimensional Angle of Arrival (2D-AoA)-azimuth and elevation, and (3) geometry-based estimation of MS position. The primary contributions of this work are as follows:

- **Channel Modeling:** a five-dimensional mmWave mMIMO channel model, considering 2D-AoD, 2D-AoA, and ToA. We propose the use of a Uniform Circular Array (UCA), which allows the inclusion of elevation angles in the steering vector.
- **Parameter Estimation:** a joint estimation of five localization parameters, including ToA, 2D-AoD, and 2D-AoA. First, we establish a mapping basis for 2D-AoA and 2D-AoD, then we use a Compressed Sensing (CS) method to map sparse mmWave signals onto our established mapping basis.
- **Localization Algorithms:** two geometry-based localization algorithms. The first focuses on LoS scenarios and utilizes ToA and 2D-AoD. The second, tailored for NLoS scenarios, employs Simultaneous Localization and Mapping (SLAM) techniques using ToA, 2D-AoD, and 2D-AoA.
- **Comprehensive Simulation Scenario:** a realistic simulation framework that incorporates LoS and NLoS conditions, mmWave and mMIMO technologies, 5G small cell indoor environments, and practical applications such as Industry-4.0 use cases.

To the best of our knowledge, this is the first work to propose a geometry-based localization method that achieves sub-metric accuracy using only one BS with a mMIMO antenna array, relying only on the existing cellular network infrastructure. Combining a novel five-dimensional mmWave mMIMO channel model, a joint estimation of localization parameters, and geometry-based algorithms tailored for both LoS and NLoS scenarios, this approach overcomes key limitations present in the state-of-the-art, such as methods assisted by Global Positioning System (GPS) or dependency on multiple Base Stations. Additionally, the proposed realistic simulation framework provides valuable insights for the academy and industry deploying localization solutions in 5G small-cell indoor environments, particularly for Industry-4.0 applications.

The remainder of this paper is organized as follows: in Section 2, a literature review is presented; in Section 3, the system model is described; in Section 4, the proposed localization method is developed; in Section 5, simulations and comparisons are presented, and the results are discussed; finally, the conclusions are drawn in Section 6.

2 | Related Works

Recent advances in edge intelligence and IoT systems highlight the growing importance of efficient localization methods in dynamic and resource-constrained environments. For instance, edge-enabled frameworks and immersive media transmission, such as those proposed in [20–23], explore collaborative task scheduling, resource optimization, and caching strategies to improve system efficiency in IoT networks. Similarly, transcoding-based approaches for video delivery [21, 22] and hierarchical game-theoretic methods for robotic task allocation [24] emphasize the critical role of accurate context-awareness, which often relies on robust localization data. Moreover, the Viewing Area Adaptive Control in Immersive Media (VAAC-IM) framework [23] focuses on adaptive control in immersive media, leveraging statistical inferences to optimize user experience and reduce redundant data transmission. While these works primarily focus on system-level optimizations, they underline the demand for precise and adaptive localization techniques, particularly in edge and IoT contexts. To review the state-of-the-art in localization methods enabling advanced applications, this section details the main works on channel modeling, parameter estimation, and localization algorithms.

Localization methods can be classified into two groups. First, those that are applied only to environments under a LoS condition, as in [25, 26]. Second, those that are applied to environments under NLoS condition, as in [18, 27, 28]. In addition, some methods estimate, as a first stage, the localization parameters (ToA, AoA, AoD) and then, as a second stage, apply a localization method, such as the proposals found in [1, 4]. Other works consider localization parameters as known input and propose only MS localization algorithms, such as those found in [18, 28].

WiFi, Bluetooth, and Ultra-Wideband (UWB) methods for indoor environments stand out for achieving sub-metric accuracy [29, 30]. However, these technologies require dedicated physical infrastructure [31–34]. On the other hand, the cellular network has the advantage of having wide coverage and being available in both outdoor and indoor environments. Some works propose localization methods using a single BS of the cellular network, such as those found in [18, 28, 35].

In [18], the authors use the single bounce (one reflection point between BS and MS) scattering model, obtaining the MS position based on the ToA, AoD, and AoA parameters. Through geometry-based relations between the Cartesian coordinates of MS, BS, and Scatterers (SCs), the authors developed a method for MS localization in NLoS conditions using the Taylor series. In [28], the author also proposes a geometry-based method. For such a purpose, he derives an algorithm to determine the intersection point among lines drawn based on AoA and AoD. In [35], instead of determining the intersection point among lines, the authors utilize a set of geometry-based formulations to propose a three-dimensional least-squares positioning technique that incorporates two or more NLoS paths.

None of the MS localization methods summarized in this section checks the LoS or NLoS condition of propagation paths. Furthermore, although the methods in [18] and [35] are fast in terms of execution time, they do not estimate the positions of the SCs. The method described in [28] estimates the positions of the SCs, but it exhibits slower execution compared to the other two methods. Therefore, there is still a need for a fast and accurate 3D method for MS localization under both LoS and NLoS conditions.

In recent works, such as [36], the authors employ an iterative weighted least-squares algorithm to estimate the MS localization in NLoS environments. The method utilizes previously estimated parameters, such as ToA, AoD, and AoA, rather than deriving them through channel modeling, which may limit its adaptability to environments with dynamic propagation conditions. Similarly, in [37], the authors propose an end-to-end approach for SLAM using mmWave signals. However, the method does not perform LoS detection and is limited to 2D environments, which restricts its applicability in scenarios requiring 3D positioning.

In this work, we go beyond the related works by proposing a fast, simple, and accurate geometry-based localization method. Moreover, different from some related works, our proposal does not assume random channel parameters as input to perform MS localization. We perform channel modeling to obtain parameters in a three-dimensional (3D) environment, and then we estimate the MS location. Some methods also perform channel modeling and parameter estimation, as in [1, 4, 38, 39]. However, they fall short in certain aspects, such as failing to estimate all localization parameters or not being applicable to 3D environments. Table 1 compares our proposal with some of the related works.

Table 1 is divided into three main sections: channel modeling, parameter estimation, and localization. The second column indicates whether or not the respective article proposes channel modeling. The third to fifth columns show which localization parameters are estimated (ToA, 2D-AoD, and 2D-AoA). From the sixth to the ninth column, aspects related to localization are highlighted, respectively, explicitly indicating whether the localization can be performed in a 3D environment, whether there is a way to detect LoS conditions, and whether the method applies to LoS or NLoS conditions. We offer a comprehensive proposal that addresses aspects not yet encompassed by other methods.

3 | System Model

This paper considers an indoor scenario based on the 3rd Generation Partnership Project (3GPP) guidelines released in the TR 38.901 V17.0.0 [40]. Figure 1A shows a single BS (equipped with a MIMO antenna array) in a known position, K SCs, and a single MS in an unknown position. Table 2 shows the notation used in this work.

The indoor scenario depicted in Figure 1A is very likely with the deployment of small cells in 5G networks, as discussed in [41, 42]. Small cells provide a solution to boost connectivity in indoor areas that were previously uncovered by a macro network, such as airports, subway stations, industries, and other collective environments [43].

We consider downlink signals and assume a high-precision clock synchronization between the BS and MS, enabling precise ToA estimation, as also assumed in [44, 45]. In the context of 5G networks, high-precision clock synchronization between BS and MS

TABLE 1 | Related works.

		Parameter estimation			Localization			
Article	**Channel modeling**	**ToA**	**2D-AoD**	**2D-AoA**	**3D**	**LoS Detection**	**LoS Method**	**NLoS Method**
Shahmansoor et al. [1]	✓	✓	×	×	×	×	✓	✓
Wang et al. [4]	✓	✓	×	✓	✓	×	✓	✓
Shikur and Weber [18]	×	×	×	×	×	×	×	✓
Yammine et al. [25]	×	✓	×	×	×	×	✓	×
Liu et al. [26]	✓	✓	×	×	×	×	✓	×
Yu and Dutkiewicz [27]	×	×	×	×	×	×	×	✓
Wymeersch [28]	×	×	×	×	✓	×	×	✓
Wei et al. [35]	×	×	×	×	✓	×	×	✓
Zhang et al. [36]	×	×	×	×	✓	×	×	✓
Rastorgueva-Foi et al. [37]	✓	✓	×	×	×	×	✓	✓
Kakkavas et al. [38]	✓	✓	×	×	×	×	✓	✓
Conceicao and Rocha [39]	✓	✓	✓	✓	✓	×	×	×
Our Proposal	✓	✓	✓	✓	✓	✓	✓	✓

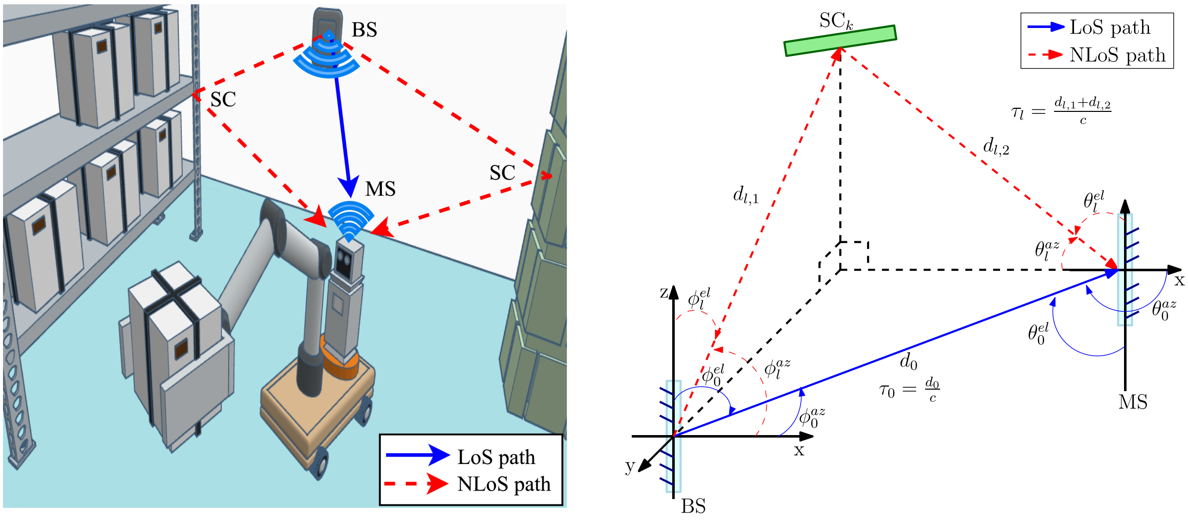

(A)

(B)

FIGURE 1 | Localization scenario with LoS and NLoS paths: **(A)** indoor scenario, **(B)** system model.

TABLE 2 | Notation.

Symbol	Description	Symbol	Description
L, K	Number of paths and SCs, respectively	d_0	Distance from BS to MS in LoS path
$d_{l,1}$	Distance from the BS to the SC associated with the *l-th* propagation path.	$d_{l,2}$	Distance from SC to MS from *l-th* path
c	Speed of light	$\boldsymbol{\tau}$	Vector of ToA
$\boldsymbol{\phi}^{az}$, $\boldsymbol{\phi}^{el}$	Vectors of azimuth and elevation angles for AoD, respectively	$\boldsymbol{\theta}^{az}$, $\boldsymbol{\theta}^{el}$	Vectors of azimuth and elevation angles for AoA, respectively
$\hat{\boldsymbol{\tau}}$	ToA obtained from the geometry-based relation and used in the Gauss-Newton algorithm	$\hat{\boldsymbol{\phi}}^{az}$, $\hat{\boldsymbol{\phi}}^{el}$	Vectors of azimuth and elevation angles for AoD, respectively, obtained from the geometry-based relation and used in the Gauss-Newton algorithm
$\hat{\boldsymbol{\theta}}^{az}$, $\hat{\boldsymbol{\theta}}^{el}$	Vectors of azimuth and elevation angles for AoA, respectively, obtained from the geometry-based relation and used in the Gauss-Newton algorithm	$\mathbf{b}$	Cartesian coordinates of the BS point in the plane
$\mathbf{m}$, $\hat{\mathbf{m}}$	Actual and estimated Cartesian coordinates of the MS location, respectively	$\mathbf{s}_k$, $\hat{\mathbf{s}}_k$	Actual and estimated Cartesian coordinates of the *k-th* SC, respectively
N_t, N_r	Number of the transmission and reception antennas, respectively	f_c	Carrier frequency
B	Bandwidth	G	Number of transmitted signals
M_t	Number of transmitted symbols per signal	$\mathbf{q}$	Vector of the transmitted symbols
N	Number of subcarriers	$\mathbf{H}$	Channel model
$\mathbf{A}_r$, $\mathbf{A}_t$	Response matrices for reception and transmission, respectively	$\mathbf{a}_r$, $\mathbf{a}_t$	Response vectors for reception and transmission, respectively
h_l	Channel gain for the l-th path	T_s	Sampling period
$\boldsymbol{\Omega}$	Element position of the UCA	$\boldsymbol{\omega}_x$, $\boldsymbol{\omega}_y$	x and y coordinates from $\boldsymbol{\Omega}$
r	Radius of the UCA	$\mathbf{K}_l$	*l-th* steering matrix
$\mathbf{y}^{(g)}[n]$	Received signal for subcarrier n and transmission g	$\mathbf{x}^{(g)}[n]$	Transmitted signal for subcarrier n and transmission g
$\mathbf{w}$	Gaussian noise	$\boldsymbol{\nu}^{az}$, $\boldsymbol{\nu}^{el}$	Vectors of candidate azimuth and elevation angles, respectively
L_{az}, L_{el}	Number of elements in $\boldsymbol{\nu}^{az}$ and $\boldsymbol{\nu}^{el}$, respectively	$\mathbf{R}_r$, $\mathbf{R}_t$	Response matrices for the AoA and AoD candidates angles, respectively
$\mathbf{z}[n]$	Sensing matrix of subcarrier n	$\check{\boldsymbol{h}}$	Recovered channel coefficients
$\dot{\boldsymbol{h}}$	Indexes of L chosen columns of the sensing matrix $\mathbf{z}[n]$	I_ϕ^l	Index for AoD in the candidate vector
ι_l^{az}, ι_l^{el}	Index for 2D-AoD angles in the candidate vector	I_θ^l	Index for AoA in the candidate vector
γ_l^{az}, γ_l^{el}	Index for 2D-AoA angles in the candidate vector	Ψ^{az}, Ψ^{el}	Opposite angles, used to verify the existence of a LoS path
Ξ	Indicates the existence of a LoS path	$\boldsymbol{\upsilon}$, $\boldsymbol{\psi}$, $\boldsymbol{\kappa}$	Auxiliary points in the Cartesian plane for the geometry-based scenario of MS localization
$\boldsymbol{\beta}_l$	Set of parameters for the *l-th* propagation path	ξ^2	Atmospheric attenuation
$\boldsymbol{\varrho}$	The complete matrix containing the final values for each iteration of the Gauss-Newton algorithm	$\boldsymbol{\varrho}_k$	The *k-th* value of the Gauss-Newton algorithm, representing the iterative correction applied to the estimated parameters
Tol	Tolerance for considering a LoS path	ξ_ϱ	Root Mean Square Error for performance evaluations
d_e	Antenna element spacing	λ_c	Wavelength
ρ_l	Pathloss for the *l-th* path	σ^2	Variance of Gaussian noise
$\mathbb{P}_0$	Poisson distribution	σ_0^2	Reflection loss

might be achieved using the generalized Precision Time Protocol (gPTP), which is based on the IEEE 802.1AS standard [46]. gPTP is a profile of the widely adopted Precision Time Protocol (PTP) defined by the IEEE 1588 standard [47].

Although gPTP/IEEE 802.1AS provides the level of synchronization required for ToA estimation, small residual timing offsets are unavoidable in practical 5G/6G deployments. Experimental studies of IEEE 802.1AS and IEEE 1588v2 have shown that hardware-timestamped synchronization typically remains within a few nanoseconds in indoor calibrated networks [46, 47]. Such timing deviations correspond to centimeter-level distance errors and are therefore significantly smaller than the geometric variations induced by LoS and single-bounce NLoS propagation.

Moreover, mmWave localization methods are known to be robust to these small offsets because the dominant source of uncertainty arises from propagation geometry rather than synchronization noise [28]. Our compressed-sensing estimator further mitigates this issue because it relies primarily on relative delays rather than absolute timing references, as also discussed in our previous work [39]. For these reasons, assuming high-precision synchronization at the system-model level is consistent with common practice in mmWave localization studies and does not compromise the validity of the proposed method.

In addition, we assume that signal propagation can occur under LoS and NLoS conditions, as depicted in Figure 1A. In the NLoS condition, MS localization requires at least two SCs, which are in unknown positions. In downlink mode, MS may receive multiple signals from SCs originating in the same BS, and each signal may be propagated using a different path. When a LoS path is available, we have a scenario with L paths and K SCs.

Figure 1B illustrates signal propagation in downlink mode using LoS and NLoS paths. In this figure, it is possible to identify parameters usually considered by the localization algorithms, where $\boldsymbol{\tau}$ represents the ToA, $\boldsymbol{\theta}$ the AoA, $\boldsymbol{\phi}$ the AoD, and indexes az and el indicate azimuth and elevation, respectively. Assuming L different paths, we generate vectors for all parameters, as follows: $\boldsymbol{\tau} = [\tau_0, \tau_1, \ldots, \tau_{L-1}]^T$, $\boldsymbol{\theta}^{az} = [\theta_0^{az}, \theta_1^{az}, \ldots, \theta_{L-1}^{az}]^T$, $\boldsymbol{\theta}^{el} = [\theta_0^{el}, \theta_1^{el}, \ldots, \theta_{L-1}^{el}]^T$, $\boldsymbol{\phi}^{az} = [\phi_0^{az}, \phi_1^{az}, \ldots, \phi_{L-1}^{az}]^T$ and $\boldsymbol{\phi}^{el} = [\phi_0^{el}, \phi_1^{el}, \ldots, \phi_{L-1}^{el}]^T$.

Moreover, in Figure 1B, d represents the Euclidean distance, c is the speed of light, and the index l refers to the l-th path. For example, assuming a NLoS path, τ_l can be determined using $d_{l,1}$ and $d_{l,2}$, where $d_{l,1}$ stands for the distance between BS and Scatterer (SC) and $d_{l,2}$ stands for the distance between SC and MS. We sort the values of $\boldsymbol{\tau} = [\tau_0, \ldots, \tau_l, \ldots, \tau_{L-1}]$ in ascending order and use l as the sort key to order θ_l^{az}, θ_l^{el}, ϕ_l^{az} and ϕ_l^{el}. In this notation, τ_0, θ_0^{az}, θ_0^{el}, ϕ_0^{az}, and ϕ_0^{el} always refer to the LoS path, if it exists.

In this work, we consider SCs as rough building walls or any natural surface present in an indoor environment. Each SC is responsible for a single-bounce specular reflection within the indoor environment. We represent location using rectangular coordinates, where x, y, and z are latitude, longitude, and altitude, respectively. Therefore, BS, MS, and SCs locations are represented by $\mathbf{b} = [b_x, b_y, b_z]^T$, $\mathbf{m} = [m_x, m_y, m_z]^T$ and $\mathbf{s}^k = [s_x^k, s_y^k, s_z^k]^T$, respectively, where $\mathbf{b}$, $\mathbf{m}$ and $\mathbf{s} \in \mathbb{R}^3$.

In accordance with widely accepted mmWave propagation characteristics, we model NLoS propagation using only first-order reflections (single-bounce). This assumption is consistent with the 3GPP TR 38.901 channel model [40], which shows that reflection losses at mmWave frequencies are significantly higher than in sub-6 GHz bands. As a consequence, higher-order reflections typically suffer compounded attenuation (due to multiple reflection events and increased path length), placing their received power close to or below the noise floor in indoor environments.

Classical mmWave measurement campaigns, such as those reported in [48], also confirm that second-order and higher-order reflections contribute negligibly to the total received power, while the dominant components are LoS and the strongest first-order NLoS paths. Recent positioning works explicitly adopt single-bounce models for these reasons. For example, the approach in [49] leverages only first-order reflections for 5G mmWave positioning and reports that higher-order components are too weak to be reliably resolved even with large bandwidths.

Therefore, restricting the propagation model to single-bounce reflections is consistent with both the standard 3GPP model and recent state-of-the-art localization methods. Including multi-bounce components would primarily increase computational complexity without offering meaningful additional information for parameter estimation or positioning accuracy.

4 | Proposed Method

Achieving precise Simultaneous Localization and Mapping (SLAM) in 3D scenarios is inherently challenging. Unlike existing methods, our approach utilizes a fast and accurate SLAM scheme by leveraging the geometry of the propagation scenario. By using channel propagation parameters, our method models the 3D space, tracing lines representing signal paths and estimating their intersection points with our algorithm based on the single-bounce scattering model, enabling fast and precise SLAM. The high accuracy of our approach, combined with its straightforward implementation, makes it a compelling solution to these challenges.

The proposed method comprises three main stages, as illustrated in Figure 2: channel modeling, parameter estimation, and MS localization. In the first stage, channel modeling is performed using mmWave mMIMO systems to characterize the communication environment and extract essential channel parameters. The second stage focuses on parameter estimation, where the key localization parameters, including ToA, 2D-AoD, and 2D-AoA, are derived using a compressed sensing-based approach. Finally, the third stage employs a geometry-based localization algorithm to determine the positions of the MS and SCs, addressing both LoS and NLoS conditions. This modular approach ensures flexibility, accuracy, and efficiency, making it suitable for diverse indoor scenarios, such as Industry 4.0 applications. Each stage is detailed in the following subsections.

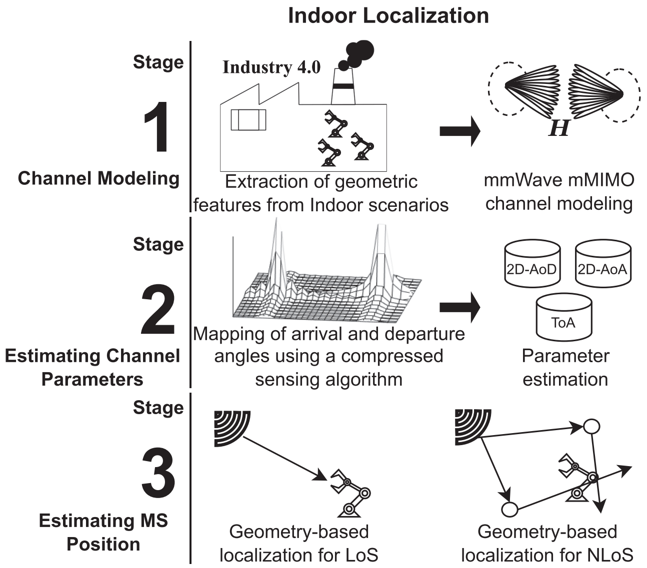

FIGURE 2 | Overview of the proposed method, comprising channel modeling, parameter estimation, and MS localization under LoS and NLoS conditions.

4.1 | Channel Modeling

Figure 1B shows channel parameters for positioning purposes. As stated in the TR 38.901 published by 3GPP [40], we consider a MIMO system with N_t transmitter antennas in the BS and N_r receiver antennas in the MS, operating at a carrier frequency f_c and bandwidth B.

Following a similar approach to [1], we consider that the BS transmits G signals to the receiver and the $g\text{-}th$ signal comprises M_t symbols transmitted in the following order: $\mathbf{q}^{(g)}[n] = [\mathbf{q}_1[n], \dots, \mathbf{q}_{M_t}[n]]^T \in \mathbb{C}^{M_t}$. In this notation, $n = 0, \dots, N-1$ represents the subcarrier index. Therefore, for the $n\text{-}th$ subcarrier, the channel matrix is written as follows:

$$\mathbf{H}[n] = \mathbf{A}_r[n]\mathbf{\Gamma}[n]\mathbf{A}_t^H[n], \tag{1}$$

where $\mathbf{A}_t$ and $\mathbf{A}_r$ are the matrices of response vectors:

$$\mathbf{A}_t[n] = [\mathbf{a}_{t,n}(\phi_0^{az}, \phi_0^{el}), \dots, \mathbf{a}_{t,n}(\phi_{L-1}^{az}, \phi_{L-1}^{el})], \tag{2}$$

$$\mathbf{A}_r[n] = [\mathbf{a}_{r,n}(\theta_0^{az}, \theta_0^{el}), \dots, \mathbf{a}_{r,n}(\theta_{L-1}^{az}, \theta_{L-1}^{el})], \tag{3}$$

and

$$\mathbf{\Gamma}[n] = \sqrt{N_t N_r} \times \text{diag}\left\{ \frac{h_0}{\sqrt{\rho_0}} e^{\frac{-j2\pi n\tau_0}{NT_s}}, \dots, \frac{h_{L-1}}{\sqrt{\rho_{L-1}}} e^{\frac{-j2\pi n\tau_{L-1}}{NT_s}} \right\}, \tag{4}$$

where ρ_l is the pathloss, h_l is the complex channel gain and $T_s = 1/B$ denotes the sampling period.

The response vectors depend on the antenna array structure. A commonly used antenna array for channel modeling is a Uniform Linear Array (ULA) [1, 4, 50]. However, as stated in [51], the use of ULA limits the estimation process to azimuth angles only. Our proposal aims to estimate not only azimuth angles but also elevation angles, thereby encompassing the 3D environment. To achieve this objective, we propose to use a UCA as follows:

$$\mathbf{a}_{t,n}(\phi_l^{az}, \phi_l^{el}) = \left[\frac{e^{-1j\pi \mathbf{\Omega}_l \mathbf{K}_l}}{\sqrt{N_t}} \right], \tag{5}$$

where $\mathbf{\Omega}_l$ is the UCA element positions, defined as:

$$\mathbf{\Omega}_l = [\boldsymbol{\omega}_{l,x}^T, \boldsymbol{\omega}_{l,y}^T], \tag{6}$$

where $\boldsymbol{\omega}_{l,x} = [rcos(\frac{2\pi(i)}{N_t})]$, and $\boldsymbol{\omega}_{l,y} = [rsin(\frac{2\pi(i)}{N_t})]$, where $i = 0, \dots, N_t - 1$. As stated in [52], the antenna radius r is determined as follows:

$$r = N_t \frac{d_e}{2\pi}, \tag{7}$$

where $d_e = \lambda_c/2$ represents the spacing of the elements, where λ_c corresponds to the wavelength. The value of $\mathbf{K}_l$ in (5) is the azimuth and elevation-dependent steering vector, defined in [51] as:

$$\mathbf{K}_l = [cos(\phi_l^{az})cos(\phi_l^{el}), sin(\phi_l^{az})cos(\phi_l^{el})]^T. \tag{8}$$

The procedure to determine the response vector $\mathbf{a}_{r,n}(\theta_l^{az}, \theta_l^{el})$ is similar to that obtained through Equations (5–8), substituting N_t by N_r and AoD ($\boldsymbol{\phi}$) by AoA ($\boldsymbol{\theta}$).

Finally, the received signal for subcarrier n and transmission g can be expressed as:

$$\mathbf{y}^{(g)}[n] = \mathbf{H}[n]\mathbf{x}^{(g)}[n] + \mathbf{w}[n], \tag{9}$$

where $\mathbf{x}^{(g)}$ is the signal with the transmitted data symbols and $\mathbf{w}$ is a Gaussian noise vector with zero mean and variance σ^2.

From (9), we estimate the parameters ToA, 2D-AoD, and 2D-AoA, using the approach presented in the following subsection.

4.2 | Estimating Channel Parameters

In order to estimate ToA ($\boldsymbol{\tau}$), 2D-AoD ($\boldsymbol{\phi}^{az}$, $\boldsymbol{\phi}^{el}$), and 2D-AoA ($\boldsymbol{\theta}^{az}$, $\boldsymbol{\theta}^{el}$), we extend the procedure demonstrated in [1], where the authors estimate ToA, 1d-AoD and 1d-AoA using Distributed Compressed Sensing Simultaneous Orthogonal Matching Pursuit (DCS-SOMP) method as presented in [53].

The DCS-SOMP method applies to signals having a sparse representation in one basis that can be recovered from a small number of projections onto a second basis. Therefore, we explore the sparsity of the mmWave mMIMO channel to recover information from each one of the received signals, according to (9).

Our estimation method differs from that of [1] by estimating 2D-AoA and 2D-AoD, instead of using a one-dimensional approach (1D-AoA and 1D-AoD). The step-by-step procedure is described as follows.

First, we define vectors as candidates to the azimuth angles $\boldsymbol{\nu}^{az} = [\nu_1^{az}, \dots, \nu_{L_{az}}^{az}]$ with L_{az} uniformly spaced values. We also define candidates to the elevation angles $\boldsymbol{\nu}^{el} = [\nu_1^{el}, \dots, \nu_{L_{el}}^{el}]$ with L_{el}

uniformly spaced values. Next, we get a response vector for each combination of the azimuth and elevation angles, obtaining the following matrices:

$$\mathbf{R}_t = [\mathbf{a}_t(\boldsymbol{\nu}^{az}, \boldsymbol{\nu}^{el})], \tag{10}$$

$$\mathbf{R}_r = [\mathbf{a}_r(\boldsymbol{\nu}^{az}, \boldsymbol{\nu}^{el})]. \tag{11}$$

The matrices $\mathbf{R}_t$ and $\mathbf{R}_r$ have dimensions $N_t \times L_{az}L_{el}$ and $N_r \times L_{az}L_{el}$, respectively. The values L_{az} and L_{el} impact the precision of the angle estimations.

To apply DCS-SOMP following a similar approach to [1], we need to jointly use $\mathbf{R}_t$, $\mathbf{R}_r$ and $\mathbf{x}^{(g)}$ (the transmitted data), obtaining the sensing matrix, as follows:

$$\mathbf{z}[n] = (\mathbf{R}_t\mathbf{x}^{(g)}[n])^T \otimes \mathbf{R}_r, \tag{12}$$

where $\otimes$ represents the Kronecker product.

Using (9) and (12) as input to the DCS-SOMP method, we obtain the recovered coefficients $\check{\boldsymbol{h}} = [\check{h}_1, \dots, \check{h}_L]$ and the respective index vector $\dot{\boldsymbol{h}} = [\dot{h}_1, \dots, \dot{h}_L]$ enabling ToA, 2D-AoA and 2D-AoD estimation.

Similar to [1], the estimation of ToA provides a maximum distance of $NT_s c$ (m). Therefore, ToA can be estimated as follows:

$$\tau_l = \check{h}_l N T_s \frac{c}{2\pi}. \tag{13}$$

With respect to the AoD estimation, first, we use $\dot{h}_l$ to determine the indexes for $\boldsymbol{\nu}^{az}$ and $\boldsymbol{\nu}^{el}$, as follows:

$$I_\phi^l = \frac{\dot{h}_l}{L_{az}L_{el}}, \tag{14}$$

$$\iota_l^{az} = \left\lfloor \frac{I_\phi^l}{L_{el}} \right\rfloor, \tag{15}$$

$$\iota_l^{el} = I_\phi^l \bmod L_{el}. \tag{16}$$

Finally, we use (15) and (16) to determine the azimuth and elevation for AoD, as follows:

$$\phi_l^{az} = \nu_{\iota_l^{az}}^{az}, \tag{17}$$

$$\phi_l^{el} = \nu_{\iota_l^{el}}^{el}. \tag{18}$$

Similarly, to estimate the AoA, we determine the indexes for $\boldsymbol{\nu}^{az}$ and $\boldsymbol{\nu}^{el}$ as follows:

$$I_\theta^l = \dot{h}_l - I_{\phi L_{az} L_{el}}^l, \tag{19}$$

$$\gamma_l^{az} = \left\lfloor \frac{I_\theta^l}{L_{el}} \right\rfloor, \tag{20}$$

$$\gamma_l^{el} = I_\theta^l \bmod L_{el}. \tag{21}$$

Finally, we use (20) and (21) to determine the azimuth and elevation for AoA, as follows:

$$\theta_l^{az} = \nu_{\gamma_l^{az}}^{az}, \tag{22}$$

$$\theta_l^{el} = \nu_{\gamma_l^{el}}^{el}. \tag{23}$$

4.3 | Estimating MS Position

Our method is tailored for LoS and NLoS conditions. First, it verifies the propagation condition to employ the most suitable algorithm for each condition. Under the LoS condition, our proposal uses ToA and AoD data to estimate the MS position. Under the NLoS condition, we jointly estimate the positions of the MS and SCs by determining the intersection point among the lines traced based on the ToA, AoD, and AoA parameters. Figure 3 highlights the three main steps to estimate the MS position, where $\boldsymbol{\upsilon}^i$, $\boldsymbol{\psi}^i$, and $\boldsymbol{\kappa}^i$ are auxiliary points used to draw the lines in the geometry-based scenario illustrated in Figure 4A,B.

Step 1) LoS algorithm: We verify the existence of a LoS path by analyzing the first values in the following vectors $\boldsymbol{\theta}^{az}$, $\boldsymbol{\theta}^{el}$, $\boldsymbol{\phi}^{az}$, and $\boldsymbol{\phi}^{el}$. From θ_0^{az}, we determine the opposite azimuth angle Ψ^{az} as follows:

$$\Psi^{az} = \begin{cases} \theta_0^{az} + \pi, & \text{if } \theta_0^{az} \leqslant 0.5\pi \\ \theta_0^{az} - \pi, & \text{if } \theta_0^{az} > 0.5\pi \end{cases} \tag{24}$$

From θ_0^{el}, we determine the opposite elevation angle Ψ^{el} as follows:

$$\Psi^{el} = \pi - \theta_0^{el}. \tag{25}$$

According to [54], a LoS path exists when $\phi_0^{az} = \Psi^{az}$ and $\phi_0^{el} = \Psi^{el}$ in the absence of angle measurement errors. Therefore, we consider an error tolerance (Tol) in angle measurement to determine the existence of a LoS path, as follows:

$$\Xi = \begin{cases} 1, & \text{if } |\phi_0^{az} - \Psi^{az}| \leqslant Tol \wedge |\phi_0^{el} - \Psi^{el}| \leqslant Tol \\ 0, & \text{if } |\phi_0^{az} - \Psi^{az}| > Tol \vee |\phi_0^{el} - \Psi^{el}| > Tol \end{cases}, \tag{26}$$

where Ξ is a binary decision variable regarding the existence or not of a LoS path, that is, $\Xi = 1$ indicates that a LoS path exists and $\Xi = 0$ indicates that only NLoS paths exist.

When the LoS path is detected ($\Xi = 1$), we estimate the MS position using the geometry-based algorithm for the LoS condition, as follows:

$$\hat{\mathbf{m}} = \mathbf{b} + \tau_0 c \begin{bmatrix} sin(\phi_0^{el})cos(\phi_0^{az}) \\ sin(\phi_0^{el})sin(\phi_0^{az}) \\ cos(\phi_0^{el}) \end{bmatrix}. \tag{27}$$

Step 2) NLoS algorithm: We determine auxiliary points in the geometry-based scenario. First, we determine the point $\boldsymbol{\upsilon}^i$ using (28). $\boldsymbol{b}$ is equidistant with respect to $\boldsymbol{\upsilon}^i$ and $\boldsymbol{m}$, passing through $\boldsymbol{s}^k$. The straight line that connects $\mathbf{b}$ and $\boldsymbol{\upsilon}^i$ crosses $\boldsymbol{s}^k$. Figure 4A depicts this scenario. Thus, $\boldsymbol{\upsilon}^i$ is determined as follows:

$$\boldsymbol{\upsilon}^i = \mathbf{b} + \tau_l c \begin{bmatrix} sin(\phi_l^{el})cos(\phi_l^{az}) \\ sin(\phi_l^{el})sin(\phi_l^{az}) \\ cos(\phi_l^{el}) \end{bmatrix}. \tag{28}$$

Second, we determine the point $\boldsymbol{\psi}^i$ using (29). The straight line that connects $\boldsymbol{\upsilon}^i$ and $\boldsymbol{\psi}^i$ crosses $\boldsymbol{m}$. Thus, $\boldsymbol{\psi}^i$ is determined as follows:

$$\boldsymbol{\psi}^i = \mathbf{b} + \tau_l c \begin{bmatrix} sin(\pi - \theta_l^{el})cos(\theta_l^{az} - \pi) \\ sin(\pi - \theta_l^{el})sin(\theta_l^{az} - \pi) \\ cos(\pi - \theta_l^{el}) \end{bmatrix}. \tag{29}$$

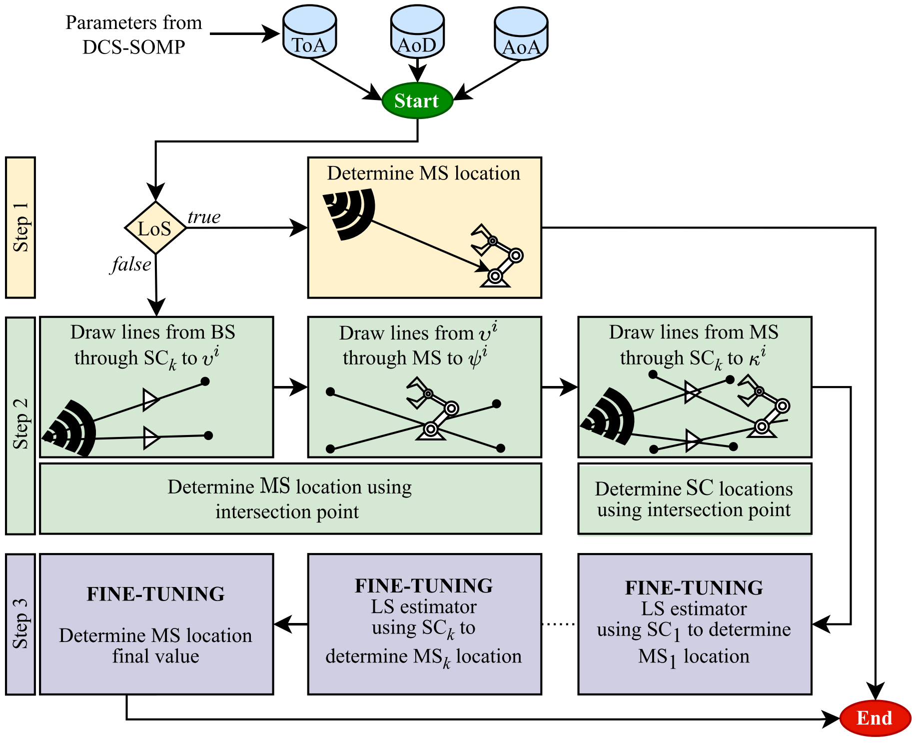

FIGURE 3 | Illustration of the steps in Stage 3: Estimating MS Position.

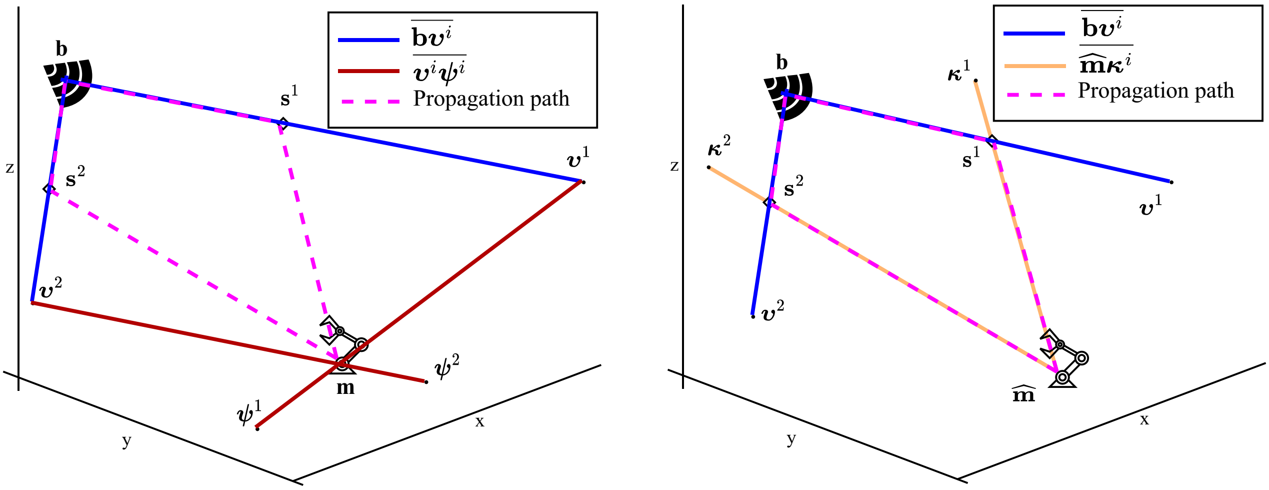

(A)

(B)

FIGURE 4 | Identifying points and lines in the NLoS scenario for **(A)** MS localization and **(B)** SC localization.

Figure 4A illustrates the drawn lines ($\overline{\mathbf{b}\boldsymbol{\upsilon}^i}$ and $\overline{\boldsymbol{\upsilon}^i\boldsymbol{\psi}^i}$) for two SCs. The intersection points among the lines $\overline{\boldsymbol{\upsilon}^i\boldsymbol{\psi}^i}$ (i.e., $\overline{\boldsymbol{\upsilon}^1\boldsymbol{\psi}^1}$ and $\overline{\boldsymbol{\upsilon}^2\boldsymbol{\psi}^2}$) corresponds to the estimated position of the MS, denoted as $\widehat{\mathbf{m}} = [\widehat{m}_x, \widehat{m}_y, \widehat{m}_z]^T$, which is determined through our proposed method. For the sake of clarity, we highlight that in Figure 4A, lines $\overline{\mathbf{b}\boldsymbol{\upsilon}^i}$ and $\overline{\boldsymbol{\upsilon}^i\boldsymbol{\psi}^i}$ do not represent the wave propagation path. They are lines that use AoA/AoD with the entire length of the ToA to create auxiliary points in the proposed geometry-based scenario. Some methods have been developed to detect the intersection point among lines using the least-squares method, as seen in [55, 56]. The method in [55] applies to scenarios with two dimensions, while in [56], to an n-dimensional space. We present an algorithm to detect the intersection point among lines in a 3D space. Our approach is specific to NLoS scenarios and demonstrates the simplicity and speed of our localization method. We detail our proposal in **Algorithm 1**.

Algorithm 1 determines the intersection point for any set of L lines, where $\mathbf{U}$ represents the set of coordinates of the starting points, and $\mathbf{V}$ stands for the coordinates of the ending points. The output variable $\mathbf{p}$ is the approximate intersection point between $\mathbf{U}$ and $\mathbf{V}$.

As long as the MS localization is determined, the estimate of the coordinates of each SC can also be obtained. To this aim, it is

ALGORITHM 1 | The intersection of lines in 3D space.

```
Input: $\mathbf{U},\mathbf{V},L$
Output: $\mathbf{p}$
$\mathbf{A} \Leftarrow \mathbf{U} - \mathbf{V}$
for i $\Leftarrow$ 1 to $L$ do
    $W \Leftarrow \sqrt{\sum_{k \Leftarrow 1}^{3} (\mathbf{A}_{i,k}^2)}$
    for j $\Leftarrow$ 1 to 3 do
        $\mathbf{A}_{i,j} \Leftarrow \frac{\mathbf{A}_{i,j}}{W}$
    end for
end for
for i $\Leftarrow$ 1 to 3 do
    for j $\Leftarrow$ 1 to 3 do
        if i=j then
            $\mathbf{H}_{i,j} \Leftarrow \sum_{k \leftarrow 1}^{L} (\mathbf{A}_{k,j}^2 - 1)$
        else
            $\mathbf{H}_{i,j} \Leftarrow \sum_{k \leftarrow 1}^{L} (\mathbf{A}_{k,i}\mathbf{A}_{k,j})$
        end if
    end for
end for
$\mathbf{C}_{1,1} \Leftarrow \sum_{i \leftarrow 1}^{L} \mathbf{U}_{i,1}\mathbf{A}_{i,1}^2 - 1 + \mathbf{U}_{i,2}\mathbf{A}_{i,1}\mathbf{A}_{i,2} + \mathbf{U}_{i,3}\mathbf{A}_{i,1}\mathbf{A}_{i,3}$
$\mathbf{C}_{2,1} \Leftarrow \sum_{i \leftarrow 1}^{L} \mathbf{U}_{i,1}\mathbf{A}_{i,1}\mathbf{A}_{i,2} + \mathbf{U}_{i,2}\mathbf{A}_{i,2}^2 - 1 + \mathbf{U}_{i,3}\mathbf{A}_{i,1}\mathbf{A}_{i,3}$
$\mathbf{C}_{3,1} \Leftarrow \sum_{i \leftarrow 1}^{L} \mathbf{U}_{i,1}\mathbf{A}_{i,1}\mathbf{A}_{i,3} + \mathbf{U}_{i,2}\mathbf{A}_{i,1}\mathbf{A}_{i,2} + \mathbf{U}_{i,3}\mathbf{A}_{i,3}^2 - 1$
$\mathbf{p} \Leftarrow (\mathbf{H}^T\mathbf{H})^{-1}\mathbf{H}^T\mathbf{C}$
return $\mathbf{p}$
```

necessary to add the point $\boldsymbol{\kappa}^i = [\kappa_x^i, \kappa_y^i, \kappa_z^i]^T$ to the geometry-based scenario. The straight line that connects $\widehat{\mathbf{m}}$ and $\boldsymbol{\kappa}^i$ crosses the SC. Thus, $\boldsymbol{\kappa}^i$ is determined as follows:

$$\boldsymbol{\kappa}^i = \widehat{\mathbf{m}} - \tau_l c \begin{bmatrix} sin(\pi - \theta_l^{el})cos(\theta_l^{az} - \pi) \\ sin(\pi - \theta_l^{el})sin(\theta_l^{az} - \pi) \\ cos(\pi - \theta_l^{el}) \end{bmatrix}. \tag{30}$$

As illustrated in Figure 4B, the intersection point among lines $\overline{\mathbf{b}\boldsymbol{\upsilon}^i}$ and $\overline{\widehat{\mathbf{m}}\boldsymbol{\kappa}^i}$ is the estimated position for the SC, $\widehat{\mathbf{s}}^k = [\widehat{s}_x^k, \widehat{s}_y^k, \widehat{s}_z^k]$, determined through **Algorithm 1**.

Step 3) Fine-tuning for NLoS condition: fine-tuning of the MS and SC estimates may be necessary, for increased accuracy, only under the NLoS condition. In order to improve the estimates found using **Algorithm 1**, we use an iterative least-squares (LS) algorithm based on the Gauss-Newton method presented in [57].

The least-squares algorithm is executed for each SC. Therefore, we define the vector $\boldsymbol{\beta}_l = [\tau_l, \theta_l^{az}, \theta_l^{el}, \phi_l^{az}, \phi_l^{el}]^T$, while MS and SC initial estimates are grouped in another vector $\boldsymbol{\varrho}_k^0 = [\widehat{m}_x, \widehat{m}_y, \widehat{m}_z, \widehat{s}_x^k, \widehat{s}_y^k, \widehat{s}_z^k]^T$.

The iterative least-squares algorithm can be defined using the following:

$$\boldsymbol{\varrho}_k^o = \boldsymbol{\varrho}_k^{o-1} + (\mathbf{J}^T\mathbf{J})^{-1}\mathbf{J}^T[\boldsymbol{\beta}_l - \mathbf{f}(\boldsymbol{\varrho}_k^{o-1})], \quad o = 2, 3, \ldots \tag{31}$$

where $\mathbf{J}$ is the Jacobian matrix $\frac{\partial \mathbf{f}(\boldsymbol{\varrho}_k^{o-1})}{\partial \boldsymbol{\varrho}_k^{o-1}}$. The vector $\mathbf{f}(\boldsymbol{\varrho}_k^{o-1}) = [\widehat{\boldsymbol{\tau}}_k, \widehat{\theta}_k^{az}, \widehat{\theta}_k^{el}, \widehat{\phi}_k^{az}, \widehat{\phi}_k^{el}]$ is determined using formulations similar to those presented in [18, 35] for NLoS condition, as follows:

$$\widehat{\tau}_k = \frac{\|\widehat{\mathbf{s}}_k - \mathbf{b}\| + \|\widehat{\mathbf{s}}_k - \widehat{\mathbf{m}}\|}{c}, \tag{32}$$

$$\widehat{\theta}_k^{az} = atan\left(\frac{\mathbf{s}_y^k - m_y}{\widehat{s}_x^k - \widehat{m}_x}\right), \tag{33}$$

$$\widehat{\theta}_k^{el} = \frac{\pi}{2} - atan\left(\frac{\widehat{s}_z^k - \widehat{m}_z}{\sqrt{(\widehat{s}_x^k - \widehat{m}_x)^2 + (\widehat{s}_y^k - \widehat{m}_y)^2}}\right), \tag{34}$$

$$\widehat{\phi}_k^{az} = atan\left(\frac{\widehat{s}_y^k - b_y}{\widehat{s}_x^k - b_x}\right), \tag{35}$$

$$\widehat{\phi}_k^{el} = \frac{\pi}{2} - atan\left(\frac{\widehat{s}_z^k - b_z}{\sqrt{(\widehat{s}_x^k - b_x)^2 + (\widehat{s}_y^k - b_y)^2}}\right). \tag{36}$$

For the best understanding of the MS and SC localization, we write $\boldsymbol{\varrho}$ in matrix form, as follows:

$$\boldsymbol{\varrho} = \begin{bmatrix} \varrho_{1,1} & \varrho_{1,2} & \cdots & \varrho_{1,K} \\ \varrho_{2,1} & \varrho_{2,2} & \cdots & \varrho_{2,K} \\ \varrho_{3,1} & \varrho_{3,2} & \cdots & \varrho_{3,K} \\ \varrho_{4,1} & \varrho_{4,2} & \cdots & \varrho_{4,K} \\ \varrho_{5,1} & \varrho_{5,2} & \cdots & \varrho_{5,K} \\ \varrho_{6,1} & \varrho_{6,2} & \cdots & \varrho_{6,K} \end{bmatrix} \begin{matrix} \left.\vphantom{\begin{matrix} a \\ a \\ a \end{matrix}}\right\} \texttt{MS Localization} \\ \left.\vphantom{\begin{matrix} a \\ a \\ a \end{matrix}}\right\} \texttt{SC Localization} \end{matrix} \tag{37}$$

where each column is the result from (31) for the *k-th* SC. Then, we determine the final location for each SC as follows:

$$\widehat{\mathbf{s}}_k = \boldsymbol{\varrho}_{4:6,k} \quad k = 1, 2, \ldots, K. \tag{38}$$

For MS Localization, we have K different values. Therefore, the final MS location is obtained as follows:

$$\widehat{\mathbf{m}} = \frac{1}{K}\sum_{k=1}^{K} \boldsymbol{\varrho}_{1:3,k}. \tag{39}$$

Algorithm 2 summarizes step-by-step the localization method proposed in this work. In Appendix A, we present numerical examples for the localization algorithms (LoS and NLoS) proposed in this work.

4.4 | Practical Considerations: Antenna Calibration and Hardware Impairments

In practical 5G deployments, UCAs naturally exhibit hardware imperfections such as mutual coupling, RF-chain gain and phase mismatches, and small geometric deviations in element positioning. These nonidealities distort the ideal steering vectors and may introduce bounded biases in the estimation of AoA, AoD, and ToA. Recent works have shown that mmWave massive MIMO systems remain robust under realistic calibration errors and that

ALGORITHM 2 | MS and SC localization.

```
Input: $\tau, \theta^{az}, \theta^{el}, \phi^{az}, \phi^{el}, \mathbf{b}, L$
Output: $\hat{\mathbf{m}}, \hat{\mathbf{s}}$
$\hat{\mathbf{m}} \Leftarrow [\ ]$
$\hat{\mathbf{s}} \Leftarrow [\ ]$
Calculate $\Xi$ using (26)
if $\Xi = 1$ then
    Calculate $\hat{\mathbf{m}}$ using (27)
else
    if $L > 1$ then
        for i $\Leftarrow$ 1 to $L$ do
            Calculate $\boldsymbol{\upsilon}^i$ using (28)
            Calculate $\boldsymbol{\psi}^i$ using (29)
        end for
        $\mathbf{U} \Leftarrow \boldsymbol{\upsilon}$
        $\mathbf{V} \Leftarrow \boldsymbol{\psi}$
        Using $\mathbf{U}$, $\mathbf{V}$ and $L$ as input, calculate $\hat{\mathbf{m}}$
         using **Algorithm 1**                                  ▷ $L$ lines
        $\mathbf{U} \Leftarrow [\hat{\mathbf{m}}, \mathbf{b}]$
        for i $\Leftarrow$ 1 to $L$ do
            Calculate $\boldsymbol{\kappa}^i$ using (30)
            $\mathbf{V} \Leftarrow [\boldsymbol{\upsilon}^i, \boldsymbol{\kappa}^i]$
            $q_l \Leftarrow 2$             ▷ Number of lines to
                           determine intersection point
            Using $\mathbf{U}$, $\mathbf{V}$ and $q_l$ as input,
              calculate $\hat{\mathbf{s}}_i$ using **Algorithm 1**
            $\boldsymbol{\beta}_i \Leftarrow [\tau_i, \theta_i^{az}, \theta_i^{el}, \phi_i^{az}, \phi_i^{el}]^T$
            $\boldsymbol{\varrho}_i^0 \Leftarrow [\hat{m}_x, \hat{m}_y, \hat{m}_z, \hat{s}_x^i, \hat{s}_y^i, \hat{s}_z^i]^T$
            Calculate the final values for $\boldsymbol{\varrho}_i$ using (31)
        end for
    end if
    Calculate the final value for $\hat{\mathbf{s}}$ using (38)
    Calculate the final value for $\hat{\mathbf{m}}$ using (39)
end if
return $\hat{\mathbf{m}}, \hat{\mathbf{s}}$
```

modern calibration techniques can effectively compensate for these impairments. For example, [58] demonstrates that realistic phase/gain errors in TDD mmWave massive MIMO can be efficiently mitigated using advanced reciprocity calibration. Likewise, in-situ Bayesian calibration has been shown to correct array distortions and mutual-coupling effects in multiport antenna systems designed for high-precision DoA estimation [59].

Specifically for UCAs, recent results in [60] indicate that circular-array auto-calibration and wideband dictionary refinement can successfully incorporate coupling-aware corrections and element-position perturbations. These findings confirm that the impact of such hardware impairments remains moderate and that UCA-based localization schemes can reliably operate under realistic conditions. Our approach follows the widely adopted assumption of a calibrated UCA, but it remains compatible with these calibration procedures, and corrected steering vectors can be incorporated without requiring structural modifications to the proposed method.

4.5 | Expected Impact of Antenna Imperfections

As discussed in the previous subsection, practical antenna arrays inevitably exhibit nonidealities such as mutual coupling, RF-chain gain/phase mismatches, and small geometric perturbations. Here, we briefly discuss their expected impact on the accuracy of the proposed localization method.

Experimental studies in mmWave systems indicate that these imperfections typically introduce mild distortions in the steering vectors, resulting in small biases in AoA/AoD estimation-often within a few degrees under indoor conditions [58, 59]. Recent calibration frameworks specifically developed for UCAs [60] further show that coupling-aware correction can restore near-ideal angular responses even when moderate array distortions are present.

In the context of our compressed-sensing estimator, these imperfections primarily affect the amplitude of the angular candidates, while the dominant grid indices corresponding to the true propagation directions remain stable. As a result, the overall effect of realistic hardware imperfections is a moderate increase in angular estimation error and, consequently, centimeter-level deviations in position estimates for typical indoor ranges. These deviations remain comparable to those reported in the mmWave localization literature and do not alter the performance trends presented in this work.

4.6 | Computational Complexity Analysis

The computational cost of the proposed method is dominated by the compressed-sensing (CS)-based parameter estimation stage. Following classical complexity derivations for sparse-recovery algorithms [61, 62], the dominant factor is the size of the angular dictionary. Let L_{az} and L_{el} denote the azimuth and elevation grid sizes, respectively, and let $q_c = L_{az} L_{el}$ represent the total number of angular candidates.

1) CS-based parameter estimation: For each subcarrier and transmitted signal, the algorithm evaluates correlations against all dictionary atoms. Since each steering-vector operation depends linearly on the antenna array size, the CS stage scales as

$$\mathcal{O}\left(N\ G\ q_c\ (N_t + N_r)\right). \tag{40}$$

2) Geometry-based localization: The LoS estimator performs only closed-form geometric operations, whose cost increases linearly with the number of paths:

$$\mathcal{O}(L). \tag{41}$$

For NLoS cases, Gauss-Newton refinement introduces an additional dependence on the number of iterations I:

$$\mathcal{O}(I\ \ L). \tag{42}$$

Since I is small in practice, this contribution remains negligible compared to the CS stage.

3) Overall complexity: The total computational complexity is therefore dominated by the CS stage and can be summarized as

$$\mathcal{O}\left(N\ G\ L_{az}L_{el}\ (N_t + N_r)\right). \tag{43}$$

This is consistent with scalability trends reported for dictionary-based mmWave parameter-estimation frameworks and explains the runtime behavior observed in the experiments.

Relation to our previous work: A more detailed complexity analysis for a related sparse-recovery framework was presented in our previous work [39], where explicit expressions were derived for the number of arithmetic operations involved in dictionary construction and correlation evaluation. The scaling behavior reported there aligns with the complexity laws derived in this section, reinforcing the validity of the computational model used in this work.

5 | Performance Evaluation

In this paper, we carried out simulations using MATLAB R2021b software[1] installed in a computer running Windows 11 as the operating system and with the following hardware configurations: 2.5 GHz Intel Core i5-10300H processor, 16 GB RAM, and NVIDIA GTX 1650 as the dedicated video card. For details about our method, please access the source code, which is publicly available in the GitHub repository.[2]

We consider an indoor environment with a length of 20 m, a width of 10 m, and a height of 5 m, as depicted in Figure 5. The experiments followed the 3GPP TR 38.901 V17.0.0 guidelines, and the protocol information adhered to the gPTP standard, based on the IEEE 802.1AS, for high-precision clock synchronization. This synchronization is critical for accurate ToA estimation in 5G networks. We consider a single-bounce setup, which can include a LoS path and several single-bounce NLoS paths. Multiple-bounce paths are not considered due to their weak reception at mmWave frequencies [38]. We have arbitrarily chosen the main simulation settings presented in Table 3. In the simulation, we define values for $\mathbf{b}$, $\mathbf{m}$, and $\mathbf{S}^k$ based on our arbitrary selection shown in Table 3. From these values, we calculate $\boldsymbol{\tau}$, $\boldsymbol{\theta}^{az}$, $\boldsymbol{\theta}^{el}$, $\boldsymbol{\phi}^{az}$, and $\boldsymbol{\phi}^{el}$ using (32–36), respectively. The positions of BS, MS, and SCs were initially defined as per Table 3, and randomized in subsequent iterations to test robustness under varying configurations. This randomization follows a Poisson distribution, represented by $\mathbb{P}_0(d_{l,2})$, as detailed in (44).

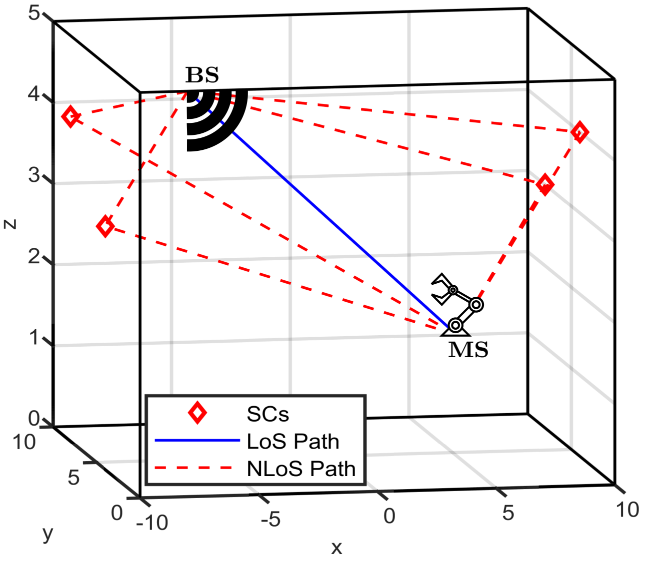

FIGURE 5 | Indoor scenario with a single BS, four SCs, and a single MS.

Additionally, parameters such as antenna spacing, SC density, and propagation conditions were varied to simulate realistic deployment scenarios.

The pathloss for each l-th path, as described in [1], is defined as follows:

$$1/\rho_l = \sigma_0^2 \mathbb{P}_0(d_{l,2}) \xi^2(d_l) \left(\frac{\lambda_c}{4\pi d_l} \right)^2, \tag{44}$$

where σ_0^2 represents the reflection loss, $\mathbb{P}_0(d_{l,2}) = (\gamma_r d_{l,2})^2 e^{-\gamma_r d_{l,2}}$ represents the Poisson distribution used to model the positions of scenario elements, such as SCs and BSs with a density of $\gamma_r = 1/7$ [1], $\xi^2(d_l)$ denotes the atmospheric attenuation over the distance $d_l = d_{l,1} + d_{l,2}$, and $(\lambda_c/4\pi d_l)^2$ represents the free space pathloss. For the LoS path, we determine:

$$1/\rho_0 = \xi^2(d_0) \left(\frac{\lambda_c}{4\pi d_0} \right)^2. \tag{45}$$

Similarly to in [1], we use $\sigma_0^2 = -10$ dB and $\xi^2(d_l) = 16$ dB/km.

We assume the Root Mean Square Error (RMSE) as the Key Performance Indicator (KPI) for our estimates. The RMSE ξ_ϱ is calculated as follows:

$$\xi_\varrho = \sqrt{\frac{1}{Q} \sum_{i=1}^{Q} \|\varrho_i - \tilde{\varrho}_i\|_2^2}, \tag{46}$$

where Q is the number of runs, ϱ_i is the vector of actual values of the chosen parameter at the i-th run, and $\tilde{\varrho}_i$ is the vector of the estimated values of the chosen parameter at the i-th run.

In addition, the RMSE was computed under various scenarios, including randomized BS, MS, and SC positions, error tolerances, and noise levels to simulate real-world conditions. These variations allowed us to evaluate the robustness of the proposed method and its adaptability to different indoor environments.

5.1 | Simulation Results

Initially, we show the impact of varying the number of antennas (Figure 6A,B) on the performance of the proposed parameter estimator. Next, we evaluate the performance of the estimator as a

TABLE 3 | Main simulation settings for generating Figures 5–8.

Parameter	Value	Parameter	Value
f_c	28 GHz	B	100 MHz
N	20	N_t	64
N_r	64	M_t	20
ν^{az}	$[0 : \pi]$	ν^{el}	$[0 : \frac{\pi}{2}]$
L_{az}	12	L_{el}	12
Tol	0.5	BS position	$\mathbf{b} = (-8, 0, 5)$
			$\mathbf{S}^1 = (-10, 4, 3)$
			$\mathbf{S}^2 = (-10, 8, 4)$
			$\mathbf{S}^3 = (10, 8, 3)$
MS position	$\mathbf{m} = (7, 10, 1)$	SC Position	$\mathbf{S}^4 = (10, 4, 4)$

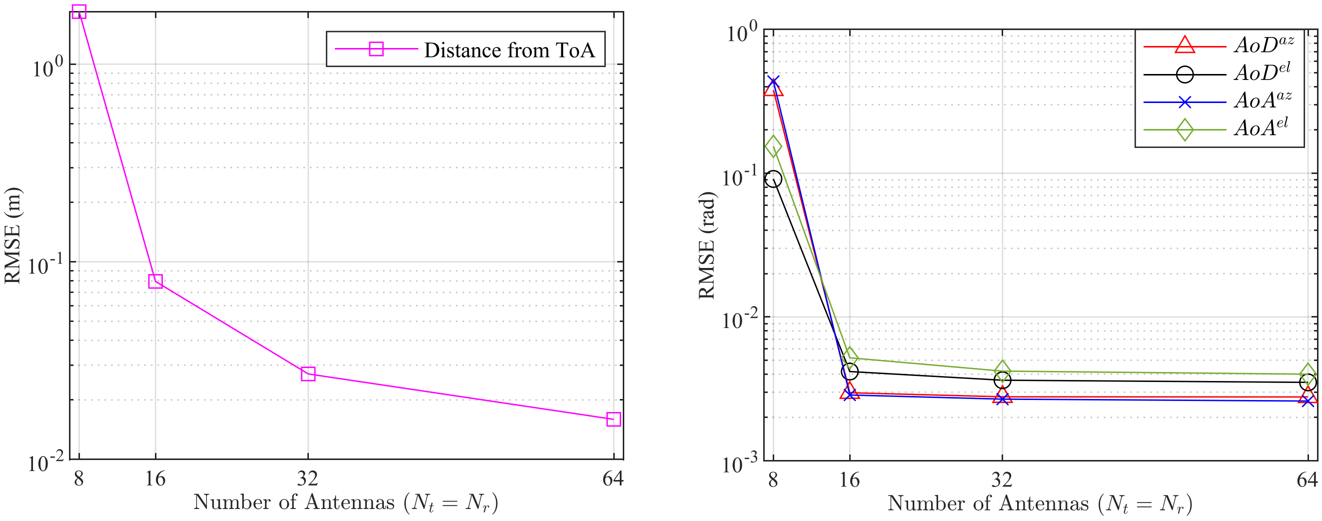

(A)

(B)

FIGURE 6 | RMSE concerning the number of antennas for the estimation of the parameters. (A) RMSE for the distance of ToA, (B) RMSE for 2D-AoD and 2D-AoA.

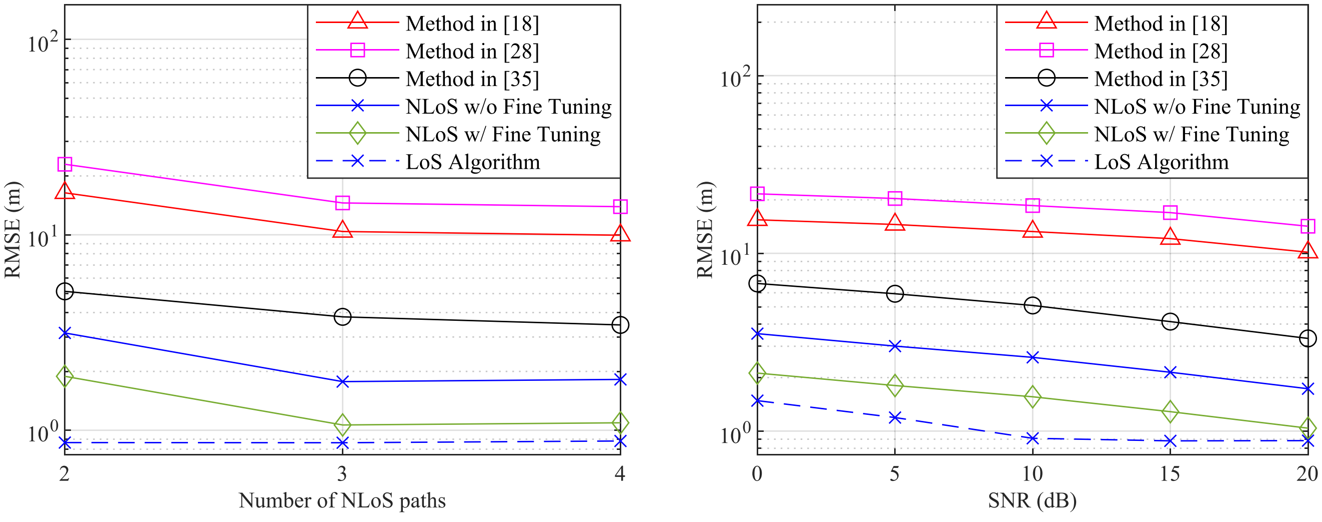

(A)

(B)

FIGURE 7 | RMSE of various NLoS algorithms compared to the LoS algorithm under varying conditions: **(A)** number of propagation paths and **(B)** SNR. The results represent the average of 1000 simulations.

function of the conditions of the communication channel, that is, varying the SNR values (Figure 7B). These simulations present results from stages 1 and 2 of our method, that is, channel modeling and parameter estimation. Finally, we evaluate the results of the localization algorithm (stage 3) by varying the number of NLoS paths considered in the indoor scenario (Figure 7A). We also evaluate the probability of success in locating the MS within an acceptable threshold for RMSE (Figure 8A). These results are complemented by those presented in the boxplot (Figure 8B) and in Table 4, including algorithms' execution time.

The analysis of Figure 6A,B shows that the RMSE of the parameters' estimates decreases as the number of antennas increases, leading us to consider mMIMO arrays to provide better accuracy for the localization methods.

We evaluate the performance of our localization method in relation to the number of paths. More specifically, we compare our proposal for the NLoS condition to those of three other methods available in the literature, which are also geometry-based approaches applied to a single BS in order to estimate the localization of MS and/or SCs. Refer to Section 2 for a brief description of the literature methods [18, 28, 35] used in this work for comparison purposes. In addition, we analyzed the impact of the use of the fine-tuning step.

In Figure 7A, we note that the NLoS localization algorithms have their accuracy improved by increasing the number of propagation paths. We also observe that our algorithms perform better than others. The LoS algorithm presents sub-metric RMSE, being, as expected, invariant to the number of NLoS paths. We

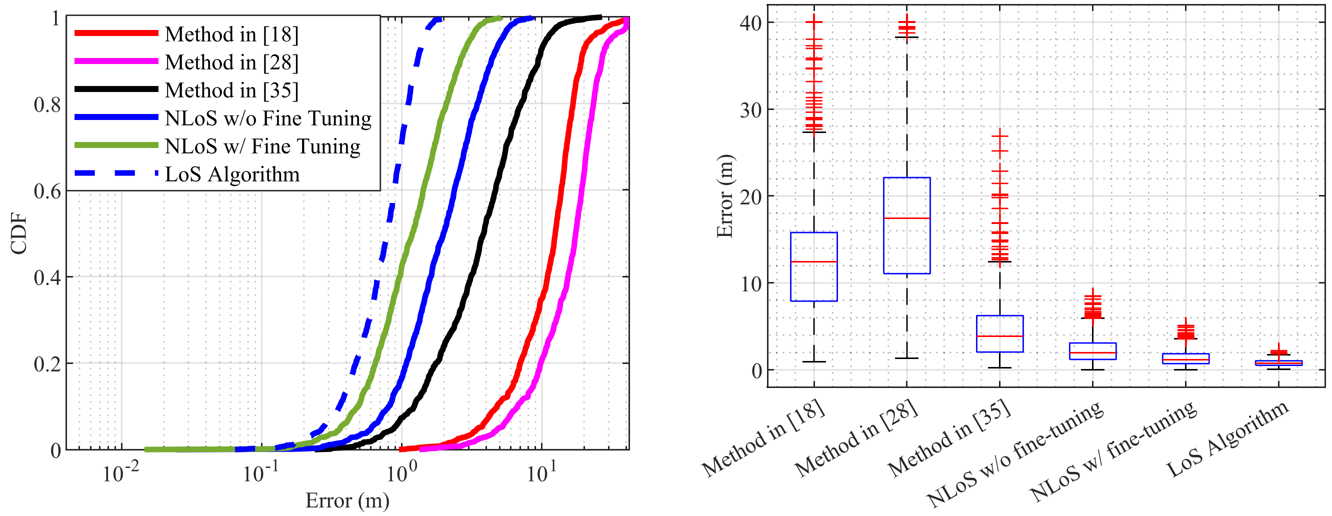

(A)

(B)

FIGURE 8 | Comparison of various NLoS algorithms with the LoS algorithm: **(A)** CDF-Localization probability and **(B)** Boxplot. The results represent the average from 1000 simulations.

TABLE 4 | Simulation results for SNR = 20 dB. Average values from 1000 simulations.

Method	**RMSE (m)**	**Accuracy in 95% (m)**	**Average runtime (s)**
Method in [18]	12.4569	21.3271	0.5033
Method in [28]	17.2494	29.8580	8.5534
Method in [35]	4.6732	10.9135	0.2053
NLoS w/o fine-tuning	2.3594	5.3847	0.1979
NLoS w/fine-tuning	1.4156	3.2308	0.8234
LoS Algorithm	0.8018	1.4486	0.1032

evaluate the performance of the algorithms in terms of SNR variation in Figure 7B. For $L = 3$, we vary the SNR from 0 to 20 dB. Note that all algorithms show better RMSE as the SNR increases. We also observe that our NLoS algorithms (with and without fine-tuning) perform better than the others and that the LoS algorithm presents sub-metric RMSE when the SNR is equal to or greater than 10 dB.

We analyze the accuracy using Cumulative Distribution Function (CDF) curves. In this case, the CDF represents the probability (axis y) that the RMSE has to assume a value less than or equal to x meters (axis x). The CDF is generated with values sorted in ascending order for 1000 independent runs. We set $L = 3$ and SNR = 20 dB. The result can be seen in Figure 8A, which shows the best performance of the proposed algorithms in relation to the others, as it presents a lower error for all probabilities.

Table 4 presents RMSE, 95% accuracy, and average runtime for the localization methods. The former two measures show lower errors by using the proposed method, and the latter shows that the proposed algorithm is also fast, enabling its implementation in real networks. Thus, the proposed method proves to be faster and more accurate than the compared methods.

Finally, we analyze the performance of our method using the boxplot shown in Figure 8B. In this representation, each box's bottom and top represent the first and third quartiles for the measured errors, respectively. In contrast, the red line represents the 50th percentile, and the cross-red marker represents the outliers, which are error values far away from other error values. The results of our method present a lower median and dispersion than the others. We also observed that our algorithms have fewer outliers than the others.

Through the results presented in this section, we observed that by using the Gauss-Newton method, our proposal presented a lower RMSE related to the MS localization in NLoS scenarios in comparison to other literature methods. Moreover, we highlight that despite using an MS localization in a 3-dimensional space, we were able to increase the accuracy of a geometry-based method while keeping its simplicity.

5.2 | Discussion: Relation to Learning-Based and Hybrid Localization Methods

Recent work on indoor positioning has explored learning-based and hybrid model-learning approaches, including deep neural networks, fingerprinting-assisted regression, and mechanisms that fuse geometric models with learned components. Surveys such as [63, 64] provide an overview of these methods and report strong performance when large annotated datasets are available.

In the mmWave domain, recent reviews [65] indicate growing interest in combining physical propagation structure with learning modules for device-based localization and sensing.

Despite their advantages, learning-based and hybrid methods typically require extensive environment-specific data collection, regular retraining when the propagation geometry changes, and may show reduced interpretability. These factors can limit their applicability in dynamic or deployment-constrained indoor scenarios.

In contrast, the method proposed in this work follows a geometry-based approach that explicitly exploits the sparse structure of mmWave propagation. This strategy offers several practical benefits: (i) it does not rely on training data or fingerprint maps; (ii) it maintains performance across different indoor layouts as long as dominant single-bounce paths can be resolved; and (iii) intermediate parameters (ToA, AoA, AoD) preserve physical meaning, facilitating diagnostics and system-level integration.

Learning-based and hybrid methods may outperform purely geometric techniques in settings with highly complex multipath or when rich labeled datasets are available. However, for the indoor mmWave scenarios considered in this work-characterized by resolvable propagation paths and limited training information-the proposed model-based framework remains an efficient, interpretable, and deployment-agnostic alternative.

6 | Conclusions

This work presented a geometry-based method for the localization of the MS and SCs using a single-bounce reflection model. The proposed method is composed of a set of procedures and algorithms that can be automatically applied to LoS and NLoS propagation conditions, as it performs a verification of the existence of a LoS path. When LoS and NLoS paths are available, the LoS algorithm is preferable to the NLoS algorithm.

Moreover, we propose a fine-tuning step using a Gauss-Newton-based algorithm to improve the geometry-based result, increasing its accuracy compared to three other geometry-based methods present in the literature. Our LoS algorithm presented sub-metric RMSE even using a single BS, while our proposals for the NLoS conditions, with and without the fine-tuning step, presented lower RMSE than the compared methods. In addition to our method's accuracy, the runtime of the algorithms based on LoS and NLoS conditions without a fine-tuning step was lower than that of the compared methods, even considering a 5G mmWave mMIMO channel. In regard to the fine-tuning step, it increases the runtime while reducing errors. The fine-tuning step is optional, however important to provide a trade-off between accuracy and runtime for different situations and scenarios.

These results are of paramount importance for 5G and B5G networks, providing enablers for many applications that are dependent on precise localization of the MS, including scenarios where the MS loses communication with neighbor cells, which may be a typical scenario for mmWave communications to users with high mobility, requiring precise localization based only on a single BS. Moreover, it also covers many scenarios of Industry-4.0, where MS in indoor environments, such as a robot, may be served by signals from a single BS deployed inside the factory.

Regarding perspectives for future studies, we aim to explore the potential of Reconfigurable Intelligent Surfaces (RIS), an emerging technology in wireless communications and localization. By incorporating RIS into the system, we expect to achieve additional improvements in localization performance by manipulating the propagation environment and optimizing communication channel characteristics. This investigation will complement our current proposals and contribute to the development of localization-specific applications that rely solely on the existing cellular infrastructure, enabling their real-world evaluation and deployment.

Acknowledgments

The authors would like to thank Fundação de Amparo à Pesquisa do Estado de Goiás (FAPEG) for the financial support. The Article Processing Charge for the publication of this research was funded by the Coordenação de Aperfeiçoamento de Pessoal de Nível Superior - Brasil (CAPES) (ROR identifier: 00x0ma614).

Funding

The authors would like to thank Fundação de Amparo à Pesquisa do Estado de Goiás (FAPEG) for the financial support.

Conflicts of Interest

The authors declare no conflicts of interest.

Data Availability Statement

Data sharing not applicable to this article as no datasets were generated or analyzed during the current study.

Endnotes

[1] Used under an academic license.

[2] https://github.com/Localization-5G/Localization.

References

1. A. Shahmansoori, G. E. Garcia, G. Destino, G. Seco-Granados, and H. Wymeersch, “Position and Orientation Estimation Through Millimeter-Wave MIMO in 5G Systems,” *IEEE Transactions on Wireless Communications* 17, no. 3 (2018): 1822–1835, https://doi.org/10.1109/TWC.2017.2785788.

2. R. Chataut and R. Akl, “Massive MIMO Systems for 5G and Beyond Networks-Overview, Recent Trends, Challenges, and Future Research Direction,” *Sensors (Basel)* 20 (2020): 2753, https://doi.org/10.3390/s20102753.

3. R. Koirala, “Joint Localization and Communication in 5G Millimeter Wave Networks,” (2020) Theses, Université Rennes 1; Università Degli Studi, Bologne, Italie.

4. Y. Wang, K. Zhao, and Z. Zheng, “An Improved 3D Indoor Positioning Study With Ray Tracing Modeling for 6G Systems,” *Mobile Networks and Applications* 28 (2023): 1162–1175, https://doi.org/10.1007/s11036-023-02127-5.

5. G. M. Mendoza-Silva, J. Torres-Sospedra, and J. Huerta, “A Meta-Review of Indoor Positioning Systems,” *Sensors* 19, no. 20 (2019): 4507, https://doi.org/10.3390/s19204507.

6. A. Fascista, A. Coluccia, H. Wymeersch, and G. Seco-Granados, “Low-Complexity Accurate Mmwave Positioning for Single-Antenna Users Based on Angle-Of-Departure and Adaptive Beamforming,” in *Proceedings of the ICASSP 2020–2020 IEEE International Conference on Acoustics, Speech and Signal Processing (ICASSP)* (IEEE, 2020), 4866–4870.

7. d J A. Peral-Rosado, R. Raulefs, J. A. López-Salcedo, and G. Seco-Granados, “Survey of Cellular Mobile Radio Localization Methods: From 1G to 5G,” *IEEE Communications Surveys and Tutorials* 20, no. 2 (2018): 1124–1148, https://doi.org/10.1109/COMST.2017.2785181.

8. O. Kanhere and T. S. Rappaport, “Position Location for Futuristic Cellular Communications: 5G and Beyond,” *IEEE Communications Magazine* 59, no. 1 (2021): 70–75.

9. T. Kim Geok, K. Zar Aung, M. Sandar Aung, et al., “Review of Indoor Positioning Radio Wave Technology,” *Applied Sciences* 11, no. 1 (2021): 279, https://doi.org/10.3390/app11010279.

10. A. Fellan, C. Schellenberger, M. Zimmermann, and H. D. Schotten, “Enabling Communication Technologies for Automated Unmanned Vehicles in Industry 4.0,” in *Proceedings of the 2018 International Conference on Information and Communication Technology Convergence (ICTC)* (IEEE, 2018), 171–176, https://doi.org/10.1109/ICTC.2018.8539695.

11. R. D. Al-kafaji, S. K. Gharghan, and S. Q. Mahdi, “Localization Techniques for Blind People in Outdoor/Indoor Environments: Review,” *IOP Conference Series: Materials Science and Engineering* 745, no. 1 (2020): 012103, https://doi.org/10.1088/1757-899X/745/1/012103.

12. W. C. S. S. Simões, G. S. Machado, A. M. A. Sales, d M M. Lucena, N. Jazdi, and d V F. Lucena, “A Review of Technologies and Techniques for Indoor Navigation Systems for the Visually Impaired,” *Sensors* 20, no. 14 (2020): 3935, https://doi.org/10.3390/s20143935.

13. Y. Li and K. Yan, “Indoor Localization Based on Radio and Sensor Measurements,” *IEEE Sensors Journal* 21, no. 22 (2021): 25090–25097, https://doi.org/10.1109/JSEN.2021.3049154.

14. W. Fang, C. Xie, and B. Ran, “An Accurate and Real-Time Commercial Indoor Localization System in LTE Networks,” *IEEE Access* 9 (2021): 21167–21179, https://doi.org/10.1109/ACCESS.2020.3034654.

15. H. Cao, Y. Wang, J. Bi, S. Xu, M. Si, and H. Qi, “Indoor Positioning Method Using WiFi RTT Based on LOS Identification and Range Calibration,” *ISPRS International Journal of Geo-Information* 9, no. 11 (2020): 627, https://doi.org/10.3390/ijgi9110627.

16. Y. Zhang, X. Tan, and C. Zhao, “UWB/INS Integrated Pedestrian Positioning for Robust Indoor Environments,” *IEEE Sensors Journal* 20, no. 23 (2020): 14401–14409, https://doi.org/10.1109/JSEN.2020.2998815.

17. K. E. Jeon, J. She, P. Soonsawad, and P. C. Ng, “BLE Beacons for Internet of Things Applications: Survey, Challenges, and Opportunities,” *IEEE Internet of Things Journal* 5, no. 2 (2018): 811–828, https://doi.org/10.1109/JIOT.2017.2788449.

18. B. Y. Shikur and T. Weber, “TDOA/AOD/AOA Localization in NLOS Environments,” in *Proceedings of the 2014 IEEE International Conference on Acoustics, Speech and Signal Processing (ICASSP)* (IEEE, 2014), 6518–6522, https://doi.org/10.1109/ICASSP.2014.6854860.

19. A. N. Bishop, B. Fidan, K. Doğançay, B. D. Anderson, and P. N. Pathirana, “Exploiting Geometry for Improved Hybrid AOA/TDOA-Based Localization,” *Signal Processing* 88, no. 7 (2008): 1775–1791.

20. H. Xiao, C. Xu, Y. Ma, S. Yang, L. Zhong, and G. M. Muntean, “Edge Intelligence: A Computational Task Offloading Scheme for Dependent IoT Application,” *IEEE Transactions on Wireless Communications* 21, no. 9 (2022): 7222–7237, https://doi.org/10.1109/TWC.2022.3156905.

21. H. Xiao, C. Xu, Z. Feng, et al., “A Transcoding-Enabled 360∘ VR Video Caching and Delivery Framework for Edge-Enhanced Next-Generation Wireless Networks,” *IEEE Journal on Selected Areas in Communications* 40, no. 5 (2022): 1615–1631, https://doi.org/10.1109/JSAC.2022.3145813.

22. H. Xiao, Y. Zhuang, C. Xu, et al., “Transcoding-Enabled Cloud-Edge-Terminal Collaborative Video Caching in Heterogeneous IoT Networks: An Online Learning Approach With Time-Varying Information,” *IEEE Internet of Things Journal* 11, no. 1 (2024): 296–310, https://doi.org/10.1109/JIOT.2023.3312916.

23. H. Xiao, C. Xu, C. Fang, S. Yang, and L. Zhong, “VAAC-IM: Viewing Area Adaptive Control in Immersive Media Transmission,” in *Proceedings of the 34th Edition of the Workshop on Network and Operating System Support for Digital Audio and Video NOSSDAV ’24* (Association for Computing Machinery, 2024), 8–14.

24. H. Xiao, Z. Huang, Z. Xu, et al., “Task-Driven Cooperative Internet of Robotic Things Crowdsourcing: From the Perspective of Hierarchical Game Theoretic,” *IEEE Internet of Things Journal* 11, no. 20 (2024): 32350–32362, https://doi.org/10.1109/JIOT.2024.3349538.

25. G. Yammine, M. Alawieh, G. Ilin, et al., “Experimental Investigation of 5G Positioning Performance Using a mmWave Measurement Setup,” in *Proceedings of the 2021 International Conference on Indoor Positioning and Indoor Navigation (IPIN)* (IEEE, 2021), 1–8, https://doi.org/10.1109/IPIN51156.2021.9662535.

26. Y. Liu, Z. Gong, Z. Zhang, et al., “High-Precision Single Base Station Localization Assisted by Beamforming,” in *Proceedings of the2021 2nd Information Communication Technologies Conference (ICTC)* (IEEE, 2021), 178–183, https://doi.org/10.1109/ICTC51749.2021.9441655.

27. K. Yu and E. Dutkiewicz, “Geometry and Motion-Based Positioning Algorithms for Mobile Tracking in NLOS Environments,” *IEEE Transactions on Mobile Computing* 11, no. 2 (2011): 254–263.

28. H. Wymeersch, “A Simple Method for 5G Positioning and Synchronization Without Line-of-Sight,” (2018). *arXiv preprint arXiv:1812.05417*.

29. A. Poulose, J. Kim, and D. S. Han, “A Sensor Fusion Framework for Indoor Localization Using Smartphone Sensors and Wi-Fi RSSI Measurements,” *Applied Sciences* 9, no. 20 (2019): 4379, https://doi.org/10.3390/app9204379.

30. A. Poulose and D. S. Han, “Hybrid Deep Learning Model Based Indoor Positioning Using Wi-Fi RSSI Heat Maps for Autonomous Applications,” *Electronics* 10, no. 1 (2021): 2, https://doi.org/10.3390/electronics10010002.

31. A. Khalajmehrabadi, N. Gatsis, and D. Akopian, “Modern WLAN Fingerprinting Indoor Positioning Methods and Deployment Challenges,” *IEEE Communication Surveys and Tutorials* 19, no. 3 (2017): 1974–2002, https://doi.org/10.1109/COMST.2017.2671454.

32. X. Hou and T. Arslan, “Monte Carlo Localization Algorithm for Indoor Positioning Using Bluetooth Low Energy Devices,” in *Proceedings of the 2017 International Conference on Localization and GNSS (ICL-GNSS)* (IEEE, 2017), 1–6, https://doi.org/10.1109/ICL-GNSS.2017.8376248.

33. A. Alarifi, A. Al-Salman, M. Alsaleh, et al., “Ultra Wideband Indoor Positioning Technologies: Analysis and Recent Advances,” *Sensors* 16, no. 5 (2016): 707, https://doi.org/10.3390/s16050707.

34. F. Zafari, A. Gkelias, and K. K. Leung, “A Survey of Indoor Localization Systems and Technologies,” *IEEE Communications Surveys and Tutorials* 21, no. 3 (2019): 2568–2599.

35. X. Wei, N. Palleit, and T. Weber, “AOD/AOA/TOA-Based 3D Positioning in NLOS Multipath Environments,” in Proceedings *of the 2011 IEEE 22nd International Symposium on Personal, Indoor and Mobile Radio Communications* (IEEE, 2011), 1289–1293, https://doi.org/10.1109/PIMRC.2011.6139709.

36. H. Zhang, H. Wymeersch, and F. Wen, “5G NLOS Positioning With Multi-Bounce Mitigation by Iterative Weighted Least Squares,” in Proceedings *of the 2023 IEEE Globecom Workshops (GC Wkshps)* (IEEE, 2023), 92–97, https://doi.org/10.1109/GCWkshps58843.2023.10465146.

37. E. Rastorgueva-Foi, O. Kaltiokallio, Y. Ge, et al., “Millimeter-Wave Radio SLAM: End-To-End Processing Methods and Experimental Validation,” *IEEE Journal on Selected Areas in Communications* 42, no. 9 (2024): 2550–2567, https://doi.org/10.1109/JSAC.2024.3413995.

38. A. Kakkavas, H. Wymeersch, G. Seco-Granados, M. H. C. García, R. A. Stirling-Gallacher, and J. A. Nossek, “Power Allocation and Parameter Estimation for Multipath-Based 5G Positioning,” *IEEE Transactions on Wireless Communications* 20, no. 11 (2021): 7302–7316.

39. D. P. F. Conceição and F. G. C. Rocha, “Adaptive DCS-SOMP for Localization Parameter Estimation in 5G Networks,” *Sensors* 23, no. 22 (2023): 9073, https://doi.org/10.3390/s23229073.

40. 3GPP, “Study on Channel Model for Frequencies From 0.5 to 100 GHz(3GPP TR 38.901 Version 17.0.0 Release 17),” (2022). Technical Specification (TS) 38.901, 3rd Generation Partnership Project (3GPP), Version 17.0.0.

41. M. H. Alsharif and R. Nordin, “Evolution Towards Fifth Generation (5G) Wireless Networks: Current Trends and Challenges in the Deployment of Millimetre Wave, Massive MIMO, and Small Cells,” *Telecommunication Systems* 64, no. 4 (2017): 617–637, https://doi.org/10.1007/s11235-016-0195-x.

42. S. Eswaran and P. Honnavalli, “Private 5G Networks: A Survey on Enabling Technologies, Deployment Models, Use Cases and Research Directions,” *Telecommunication Systems* 82, no. 1 (2023): 3–26, https://doi.org/10.1007/s11235-022-00978-z.

43. Ericsson.com, “Accelerating 5G Indoor Experiences,” (2021).

44. X. Quan, K. Niu, C. Dong, and Y. Yu, “Joint Approximate Maximum Likelihood Localization Algorithm in 5G New Radio Systems,” in *Proceedings of the 2020 IEEE 31st Annual International Symposium on Personal, Indoor and Mobile Radio Communications* (IEEE, 2020), 1–6, https://doi.org/10.1109/PIMRC48278.2020.9217380.

45. M. Pan, P. Liu, S. Liu, et al., “Efficient Joint DOA and TOA Estimation for Indoor Positioning With 5G Picocell Base Stations,” *IEEE Transactions on Instrumentation and Measurement* 71 (2022): 1–19, https://doi.org/10.1109/TIM.2022.3191705.

46. IEEE, “IEEE Standard for Local and Metropolitan Area Networks–Timing and Synchronization for Time-Sensitive Applications,” in *IEEE Std 802.1AS-2020 (Revision of IEEE Std 802.1AS-2011)* (IEEE, 2020), 1–421, https://doi.org/10.1109/IEEESTD.2020.9121845.

47. IEEE, “IEEE Standard for a Precision Clock Synchronization Protocol for Networked Measurement and Control Systems,” in *IEEE Std 1588–2008 (Revision of IEEE Std 1588–2002)* (IEEE, 2008), 1–269, https://doi.org/10.1109/IEEESTD.2008.4579760.

48. T. S. Rappaport, G. R. MacCartney, and others, *Millimeter Wave Wireless Communications* (Pearson Education, 2015).

49. Q. Bader, S. Saleh, M. Elhabiby, and A. Noureldin, “Leveraging Single-Bounce Reflections and Onboard Motion Sensors for Enhanced 5G Positioning,” *IEEE Transactions on Intelligent Transportation Systems* 25, no. 12 (2024): 20464–20477, https://doi.org/10.1109/TITS.2024.3480525.

50. L. Bai, C. Y. Peng, and S. Biswas, “Association of DOA Estimation From Two ULAs,” *IEEE Transactions on Instrumentation and Measurement* 57, no. 6 (2008): 1094–1101, https://doi.org/10.1109/TIM.2007.915122.

51. A. Manikas, *Differential Geometry in Array Processing* (Imperial College Press, 2004).

52. L. Jin, L. li, and H. Wang, “Investigation of Different Types of Array Structures for Smart Antennas,” in *Proceedings of the 2008 International Conference on Microwave and Millimeter Wave Technology*, vol. 3 (IEEE, 2008), 1160–1163, https://doi.org/10.1109/ICMMT.2008.4540633.

53. M. Duarte, S. Sarvotham, D. Baron, M. Wakin, and R. Baraniuk, “Distributed Compressed Sensing of Jointly Sparse Signals,” in *Conference Record of the Thirty-Ninth Asilomar Conference on Signals, Systems and Computers, 2005* (IEEE, 2005), 1537–1541, https://doi.org/10.1109/ACSSC.2005.1600024.

54. K. Yu and Y. J. Guo, “Statistical NLOS Identification Based on AOA, TOA, and Signal Strength,” *IEEE Transactions on Vehicular Technology* 58, no. 1 (2009): 274–286, https://doi.org/10.1109/TVT.2008.924975.

55. J. Traa, “Least-Squares Intersection of Lines,” (2013).

56. L. Han and J. C. Bancroft, “Nearest Approaches to Multiple Lines in n-Dimensional Space. CREWES Research Report,” 22 (2010).

57. P. Deuflhard, *Newton Methods for Nonlinear Problems: Affine Invariance and Adaptive Algorithms* (Springer, 2011), 173–231.

58. S. Xu, Z. Zhang, Y. Xu, C. Li, and L. Yang, “Deep Reciprocity Calibration for TDD mmWave Massive MIMO Systems Toward 6G,” *IEEE Transactions on Wireless Communications* 23, no. 10 (2024): 13285–13299, https://doi.org/10.1109/TWC.2024.3400616.

59. R. Pöhlmann, S. Zhang, E. Staudinger, S. Caizzone, A. Dammann, and P. A. Hoeher, “Bayesian in-Situ Calibration of Multiport Antennas for DoA Estimation: Theory and Measurements,” *IEEE Access* 10 (2022): 37967–37983, https://doi.org/10.1109/ACCESS.2022.3164520.

60. Z. Bozorgasl, H. Chen, and M. J. Dehghani, “Auto-Calibration and 2D-DOA Estimation in UCAs via an Integrated Wideband Dictionary,” (2024). *arXiv preprint arXiv:2404.17089*.

61. C. Qi and L. Wu, “A Hybrid Compressed Sensing Algorithm for Sparse Channel Estimation in MIMO OFDM Systems,” in *Proceedings of the 2011 IEEE International Conference on Acoustics, Speech and Signal Processing (ICASSP)* (IEEE, 2011), 3488–3491, https://doi.org/10.1109/ICASSP.2011.5946229.

62. Y. Zhou, F. Tong, A. Song, and R. Diamant, “Exploiting Spatial-Temporal Joint Sparsity for Underwater Acoustic Multiple-Input-Multiple-Output Communications,” *IEEE Journal of Oceanic Engineering* 46, no. 1 (2021): 352–369, https://doi.org/10.1109/JOE.2019.2958003.

63. V. Bellavista-Parent, J. Torres-Sospedra, and A. Pérez-Navarro, “Comprehensive Analysis of Applied Machine Learning in Indoor Positioning Based on Wi-Fi: An Extended Systematic Review,” *Sensors* 22, no. 12 (2022): 4622, https://doi.org/10.3390/s22124622.

64. K. A. Kordi, M. Roslee, M. Y. Alias, A. Alhammadi, A. Waseem, and A. F. Osman, “Survey of Indoor Localization Based on Deep Learning,” *Computers, Materials and Continua* 79, no. 2 (2024): 3261–3298, https://doi.org/10.32604/cmc.2024.044890.

65. A. Shastri, N. Valecha, E. Bashirov, et al., “A Review of Millimeter Wave Device-Based Localization and Device-Free Sensing Technologies and Applications,” *IEEE Communications Surveys and Tutorials* 24, no. 3 (2022): 1708–1749, https://doi.org/10.1109/COMST.2022.3177305.

Appendix A

Examples

In this appendix, we present numerical examples using our proposed algorithms to facilitate result reproduction and providing a detailed understanding of their functionality.

Example 1. Scenario with LoS and NLoS paths.

Figure A1 shows the scenario with LoS and NLoS paths. The BS was defined at the coordinates $\mathbf{b} = (0, 0, 10)$ and the MS at $\mathbf{m} = (20, 5, 0)$. Three SCs ($K = 3$) were used, $\mathbf{s}^1 = (15, 0, 0)$, $\mathbf{s}^2 = (-10, 15, 2)$ and $\mathbf{s}^3 = (5, -15, 5)$.

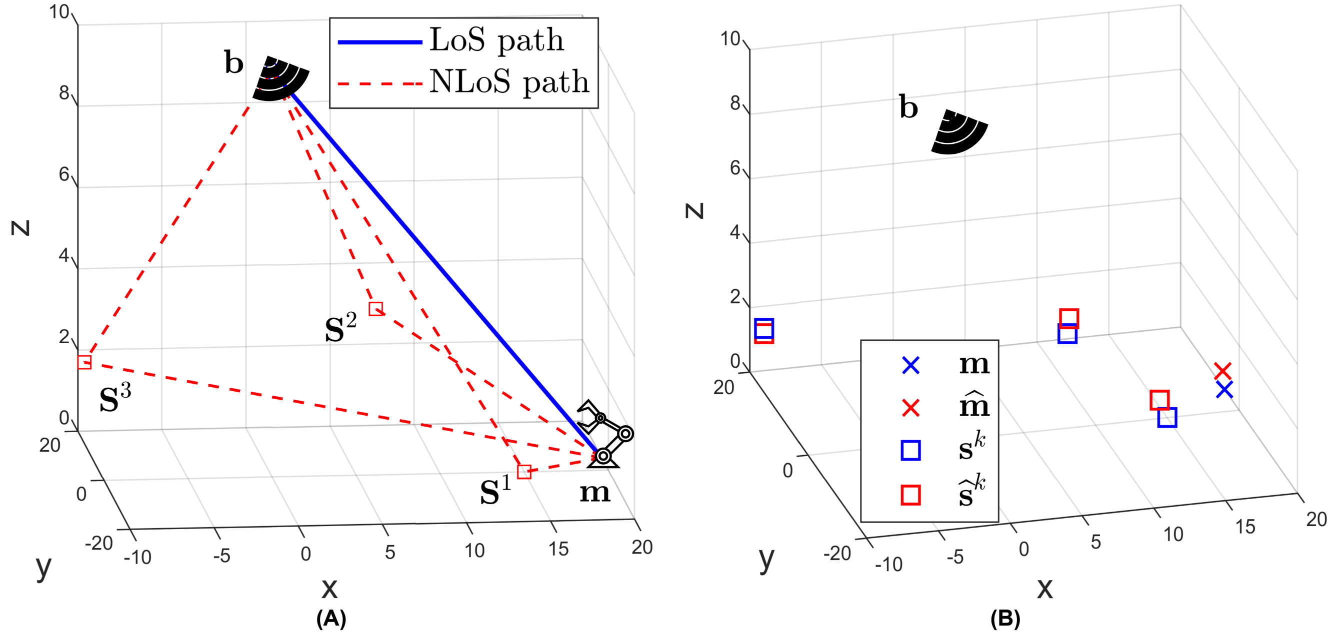

(A) (B)

FIGURE A1 | **(A)** The scenario of examples 1 and 2. **(B)** Final localization scenario showing actual and estimated positions for MS and SCs.

We determine the channel parameters, obtaining the vectors:

$$\boldsymbol{\tau}c = \begin{bmatrix} 22.97 \\ 25.21 \\ 42.09 \\ 51.34 \end{bmatrix}, \boldsymbol{\theta}^{az} = \begin{bmatrix} 3.37 \\ 3.93 \\ 2.81 \\ 4.09 \end{bmatrix}, \boldsymbol{\theta}^{el} = \begin{bmatrix} 1.12 \\ 1.56 \\ 1.49 \\ 1.37 \end{bmatrix},$$

$$\boldsymbol{\phi}^{az} = \begin{bmatrix} 0.24 \\ -0.01 \\ 2.16 \\ -1.24 \end{bmatrix} \text{ and } \boldsymbol{\phi}^{el} = \begin{bmatrix} 2.00 \\ 2.17 \\ 1.97 \\ 1.86 \end{bmatrix}.$$

Since we already determined the parameters, we set values to the variable L, in order to execute **Algorithm 2**, which detects the existence of the LoS path and determines $\hat{\mathbf{m}}$ from (27). In our example, we set $L = 4$, and then we obtained $\hat{\mathbf{m}} = (20.15, 5.13, 0.24)$. The RMSE for this MS localization is 0.31 m.

Example 2. Scenario without LoS path.

This example was carried out with the same previous configurations, taking into account only the three NLoS paths, obtaining the following vectors:

$$\boldsymbol{\tau}c = \begin{bmatrix} 25.25 \\ 41.90 \\ 51.48 \end{bmatrix}, \boldsymbol{\theta}^{az} = \begin{bmatrix} 3.92 \\ 2.82 \\ 4.06 \end{bmatrix}, \boldsymbol{\theta}^{el} = \begin{bmatrix} 1.59 \\ 1.49 \\ 1.37 \end{bmatrix},$$

$$\boldsymbol{\phi}^{az} = \begin{bmatrix} 0.01 \\ 2.16 \\ -1.24 \end{bmatrix} \text{ and } \boldsymbol{\phi}^{el} = \begin{bmatrix} 2.16 \\ 1.99 \\ 1.87 \end{bmatrix}.$$

Whether there is no LoS path, we determine $\boldsymbol{\upsilon} = [\boldsymbol{\upsilon}^1, \boldsymbol{\upsilon}^2, \boldsymbol{\upsilon}^3]$ and $\boldsymbol{\psi} = [\boldsymbol{\psi}^1, \boldsymbol{\psi}^2, \boldsymbol{\psi}^3]$ for each SC using (28) and (29), to obtain:

$$\boldsymbol{\upsilon} = \begin{bmatrix} 20.94 & -26.09 & 12.69 \\ 0.08 & 38.96 & -37.85 \\ -4.10 & -11.24 & -2.72 \end{bmatrix}, \boldsymbol{\psi} = \begin{bmatrix} 17.86 & 48.81 & 24.82 \\ 17.84 & -15.92 & 32.80 \\ 10.52 & 6.24 & 2.02 \end{bmatrix}.$$

Using the coordinates of $\boldsymbol{\upsilon}$ and $\boldsymbol{\psi}$, we have the lines of the geometry-based scenario and the intersection point among lines $\overline{\boldsymbol{\upsilon}^i\boldsymbol{\psi}^i}$ determined using **Algorithm 1**, getting $\hat{\mathbf{m}} = (20.12, 4.98, -0.12)$.

In order to estimate the locations of the SCs, we first determine $\boldsymbol{\kappa} = [\boldsymbol{\kappa}^1, \boldsymbol{\kappa}^2, \boldsymbol{\kappa}^3]$ using (30) to obtain:

$$\boldsymbol{\kappa} = \begin{bmatrix} 2.23 & -28.61 & -4.87 \\ -12.55 & 21.07 & -27.78 \\ 0.29 & 3.38 & 8.34 \end{bmatrix}.$$

By executing **Algorithm 1** for each path using lines $\overline{\mathbf{b}\boldsymbol{\upsilon}^i}$ and $\overline{\hat{\mathbf{m}}\boldsymbol{\kappa}^i}$, we get $\hat{\mathbf{s}}^1 = (15.03, 0.24, 0.17)$, $\hat{\mathbf{s}}^2 = (-10.14, 15.01, 2.14)$ and $\hat{\mathbf{s}}^3 = (4.82, -14.97, 5.19)$. The final value of $\hat{\mathbf{m}}$ is determined using (31) and (39), yielding $\hat{\mathbf{m}} = (20.05, 4.98, -0.04)$. In this case, the RMSE of MS localization is 0.07 m. By analyzing Figure A1, which illustrates the final state of the localization scenario for this example, we see that the proposed method estimates values for MS and SCs (red markers) close to the actual values (blue markers).